Materials Today Bio 25 (2024) 100996

Contents lists available at ScienceDirect

Materials Today Bio

journal homepage: www.journals.elsevier.com/materials-today-bio

Multifunctional nanomaterials *via* cell cuproptosis and oxidative stress for treating osteosarcoma and OS-induced bone destruction

Lin Ye [a,b,1], Congcong Yu [a,b,1], Jiechao Xia [a,b,1], Kainan Ni [c], Yejin Zhang [c], Xiaozhang Ying [a,b], Dingqi Xie [a,b], Yang Jin [a,b], Rongtai Sun [a,b], Ruikang Tang [d,***], Shunwu Fan [a,b,**], Shasha Yao [a,b,*]

[a] Department of Orthopaedic Surgery, Key Laboratory of Musculoskeletal System Degeneration and Regeneration Translational Research of Zhejiang Province, Sir Run Run Shaw Hospital, Medical College of Zhejiang University, Hangzhou, 310016, China
[b] Key Laboratory of Musculoskeletal System Degeneration and Regeneration, Translational Research of Zhejiang Province Hangzhou, Zhejiang, 310016, China
[c] Department of Orthopedics, Affiliated Lishui Hospital of Zhejiang University-the Fifth Medical Affiliated Hospital of Wenzhou University-Lishui Central Hospital, Lishui, 323600, China
[d] Center for Biomaterials and Biopathways, Department of Chemistry, Zhejiang University, Hangzhou, Zhejiang, 310027, China

ARTICLE INFO

Keywords:
Cuproptosis
Responsive biomaterial
Neoplastic bone destruction
Reactive oxygen species
Mild photo-thermal therapy

ABSTRACT

Reactive Oxygen Species (ROS) refers to a highly reactive class of oxidizing species that have the potential to induce cellular apoptosis and necrosis. Cuproptosis, a type of cell death, is primarily associated with the effects of copper ions. However, the specific relationship between ROS, cuproptosis, and osteosarcoma (OS) remains relatively unexplored. Additionally, there is limited research on the use of cuproptosis in conjunction with oxidative stress for treating OS and inhibiting tumor-induced bone destruction. To address these gaps, a novel treatment approach has been developed for OS and neoplastic bone destruction. This approach involves the utilization of glutathione (GSH) and pH-responsive organic-inorganic mesoporous silica nanoparticles@Cu_2S@oxidized Dextran (short for MCD). The MCD material demonstrates excellent cytocompatibility, osteogenesis, tumor suppression, and the ability to inhibit osteoclast formation. The specific mechanism of action involves the mitochondria of the MCD material inhibiting key proteins in the tricarboxylic acid (TCA) cycle. Simultaneously, the generation of ROS promotes this inhibition and leads to alterations in cellular energy metabolism. Moreover, the MCD biomaterial exhibits promising mild-temperature photothermal therapy in the second near-infrared (NIR-II) range, effectively mitigating tumor growth and OS-induced bone destruction *in vivo*.

1. Introduction

Osteosarcoma (OS) is a prevalent bone tumor, accounting for 44.6% of all bone tumors, and is associated with a poor prognosis in individuals aged 10 to 25 [1]. In clinical practice, the treatment of osteosarcoma often involves surgical intervention, radiation therapy, or a combination of both [2,3]. However, the treatment outcomes are not satisfactory for patients, especially in the case of osteosarcoma with metastasis [4,5]. The aggressive nature of OS is characterized by both local invasion and distant metastasis, primarily through its invasive and migratory capabilities, ultimately resulting in lung metastasis, which is the leading cause of mortality in OS patients [6,7]. Additionally, OS tumors can secrete significant quantities of RANK ligands (RANKLs), which promote the differentiation of precursor cells into osteoclasts, contributing to the development of pathological fractures [8–11]. Consequently, the suppression of tumor-associated osteoclast activity plays a crucial role in

* Corresponding author. Department of Orthopaedic Surgery, Key Laboratory of Musculoskeletal System Degeneration and Regeneration Translational Research of Zhejiang Province, Sir Run Run Shaw Hospital, Medical College of Zhejiang University, Hangzhou, 310016, China.
** Corresponding author. Department of Orthopaedic Surgery, Key Laboratory of Musculoskeletal System Degeneration and Regeneration Translational Research of Zhejiang Province, Sir Run Run Shaw Hospital, Medical College of Zhejiang University, Hangzhou, 310016, China.
*** Corresponding author.
E-mail addresses: rtang@zju.edu.cn (R. Tang), shunwu_fan@zju.edu.cn (S. Fan), yaoshasha@zju.edu.cn (S. Yao).
[1] These authors contributed equally to this work.

https://doi.org/10.1016/j.mtbio.2024.100996
Received 1 November 2023; Received in revised form 30 January 2024; Accepted 8 February 2024
Available online 15 February 2024

treating OS, as it is directly responsible for subsequent bone destruction in the affected area.

Copper ions can initiate cuproptosis, a cell death pathway that relies on copper and consistently disrupts mitochondrial metabolism by directly impacting the tricarboxylic acid (TCA) cycle [12]. This type of cell death, induced by copper, was first identified by Tsvetkov and is distinct from other forms of regulatory cell death (RCD) [13]. Li et al. further identified seven genes (FDX1, LIAS, LIPT1, DLD, DLAT, PDHA1, PDHB) that promote cuproptosis, as well as other three genes (MTF1, GLS, CDKN2A) that inhibit this mechanism in patients of OS [14]. These help us understand copper-induced cell death. Additionally, copper ions can generate reactive oxygen species (ROS) through the Fenton-like reaction. These ROS can function as signal transduction molecules, playing significant roles in normal cellular signaling and regulating various physiological functions [15,16]. However, when present in excessive amounts, ROS can become detrimental, leading to oxidative stress and causing cellular damage that ultimately results in cell death [17]. Despite the crucial roles that ROS and copper-induced cell death play in cellular function regulation, there have been relatively few studies exploring the synergistic treatment of biological diseases using ROS and cell cuproptosis, particularly in the context of OS and the associated bone destruction. Moreover, the potential mechanisms underlying the impact of copper ions on OS-induced osteoclasts remain poorly understood.

In this research, we utilized the combined effects of copper-induced cell death and reactive oxygen species (ROS) as a treatment approach for osteosarcoma and associated bone destruction. An organic-inorganic GSH/pH-responsive mesoporous silica-cuprous sulfide-oxidized dextran nanoparticles (referred to as MCD) was developed by coating extremely small-sized Cu_2S@BSA hybrid nanoparticles onto dendritic mesoporous silica nanoparticles (MSN) through electrostatic attraction, followed by wrapping them with oxidized dextran (oDEX) using Schiff base bonds (see Scheme 1A). In this study, oDEX plays two main roles in this study. Firstly, it forms Schiff base bonds with mesoporous silica nanoparticles (MSN-NH_2), thus blocking Cu_2S and representing the principle of material pH responsiveness. Secondly, it enhances the material's tissue compatibility. The resulting MCD nanoparticles exhibited good biocompatibility, photothermal properties, and antibacterial activity. Within the OS environment, the MSN component of MCD nanoparticles degraded and gradually released a large quantity of Cu_2S nanoparticles. These nanoparticles induced mitochondrial pathway abnormalities, ultimately resulting in the cuproptosis of tumor cells. Surprisingly, the MCD nanoparticles also generated ROS, which enhanced the sensitivity of mitochondria to cuproptosis. Moreover, the MCD nanoparticles inhibited the formation of osteoclasts by suppressing the expression of FDX1, LIAS, and DALT proteins in the tricarboxylic acid (TCA) cycle. The organic-inorganic MCD biomaterial further promoted the osteogenic differentiation of bone marrow mesenchymal stem cells (BMSCs), facilitating bone healing and calcium mineralization. In summary, we developed an innovative therapy manner by utilizing the organic-inorganic hybrid nanomaterials MCD nanoparticles which allowed for the in-situ suppression of osteosarcoma, the inhibition of osteoclasts, the prevention of bone defect development, and the inhibition of tumor metastasis (see Scheme 1B). This research will not only provide a promising strategy but also inspire some new thinking for orthotopic osteosarcoma therapy.

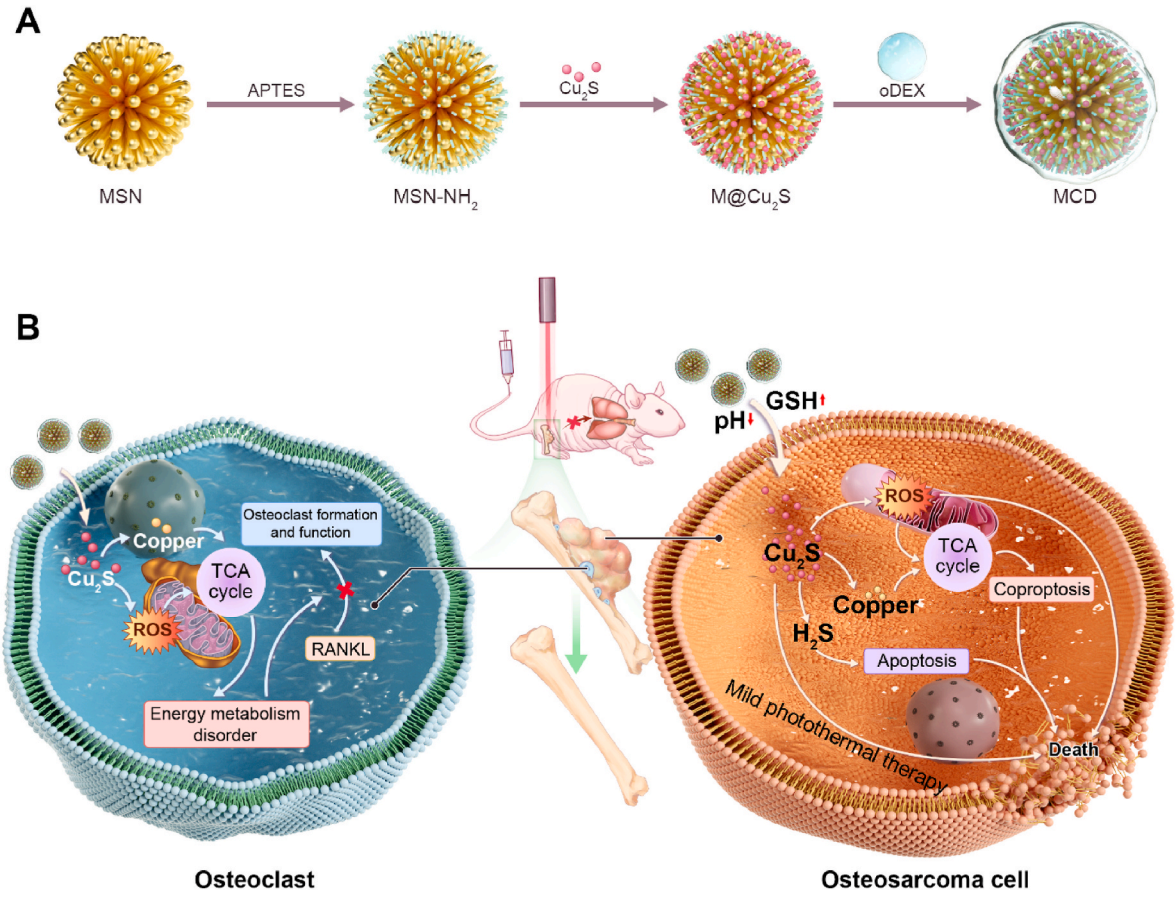

Scheme 1. Schematic illustration of the MCD nanoparticles for therapy of OS. (A) Schematic diagram of the steps for the MCD synthesis. (B) The MCD nanoparticles with the anti-tumor effects and osteoclast inhibition for OS therapy.

2. Materials and methods

2.1. Reagents and materials

$CuCl_2$, bovine serum albumin (BSA), trisodium citrate dihydrate and sodium sulfide nonahydrate ($Na_2S{\cdot}9H_2O$), sodium citrate dihydrate, tetraethyl orthosilicate, bis[3-(triethoxysilyl) propyl] tetrasulfide (BTESPTS), triethanolamine (TEA), sodium periodate ($NaIO_4$), 3-aminopropyltriethoxysilane (APTES), sodium salicylate (NaSal), hexadecyl trimethyl ammonium bromide (CTAB), dextran, and glutathione (GSH) were purchased from Aladdin.

2.2. Syntheses of Cu_2S@BSA and MSN

The preparation and synthesis of the Cu_2S@BSA have been modified based on the previous literature [18]. The Cu_2S nanoparticles were synthesized via a modified method described in the previous article. BSA solution (1 mL, 20 mg/mL) was added to the sodium citrate (5 mL, 8 mM) and $CuCl_2$ (5 mL, 8 mM) mixture for 15 min at 37 °C under vigorous stirring. Then $Na_2S{\cdot}9H_2O$ solution (5 mL, 16 mM) was added to the above materials and continued to react for 12 h. The solution was dialyzed to remove the unreacted materials with dialysis membranes (with an MWCO 100 kDa) for five days and it was freeze-dried using a lyophilizer.

Synthesis and modification of MSN: the nanoscale MSN was modified based on a previously reported method [19]. Briefly, 40 μL TEA, 0.2 g CTAB, and 63 mg NaSal were mixed in 50 mL of ddH_2O with vigorous stirring for 3 h. Then, 2 mL TEOS and 1 mL BTESPTS were dropwise added to the above solution. After reaction for 16 h, the materials were collected by centrifugation (10000 rpm, 20 min), and washed with ddH_2O three times. After centrifugation, the materials were removed from the template by hot ethanol-HCL mixture and dried at 50 °C.

To functionalize the MSN carrier with amino groups, 100 mg MSN was dissolved into 20 mL toluene with stirring for 2 h at 30 °C. Finally, 300 μL APTES was added to the above mixture and stirred for 24 h. MSN-NH_2 was collected by centrifugation (10000 rpm, 0.5 h).

2.3. Preparation of oxidized dextran (oDEX)

Typically, 5 g dextran was diluted into 200 mL ddH_2O under stirring at 50 °C. Then, 6.6 g $NaIO_4$ was dissolved into the above mixture and stirred for 12 h protected from light. The oxidizing reaction was terminated by adding 30 mL propanetriol and stirring to mix well. Similarly, the solution was dialyzed to remove unreacted materials with a dialysis membrane (MWCO 3500 Da) for five days and lyophilized.

2.4. Cu_2S@BSA loading and capping

100 mg Cu_2S@BSA and 10 mg MSN were ultrasonically dispersed in 5 mL ddH_2O, followed by stirring for 2 h at 4 °C, and then the turbid liquid was mixed at 4 °C overnight protected from light. The material was collected by centrifuge, washed by ddH_2O three times to remove excess Cu_2S@BSA, and freeze-dried by a lyophilizer.

500 mg oDEX was dissolved in 50 mL of 10 mM MES buffer (pH = 8.5) with stirring for 2 h at room temperature protected from light. Next, 25 mg MCD was put into the above mixture and kept stirring overnight. Finally, materials were collected by centrifuging and washed three times.

2.5. MD degradation experiment and Cu_2S release

To investigate the degradation of the MSN-oEDX *in vitro*, 20 mg MSN-oEDX was dispersed into 50 mL ddH_2O solution at different pH values (pH = 7.4 and 6.5), which containing GSH with different concentrations GSH (0 and 10 mM). The solutions were shaken at 300 rpm and 37 °C. Samples of MSN-oEDX were isolated after 24 and 48 h for TEM observation.

To assess the release of Cu_2S, MCD was dispersed into 50 mL PBS solution at different pH values (pH = 7.4, 6.5, and 6), which contained GSH with different concentrations (0 and 10 mM). The solutions were shaken at 300 rpm and 37 °C, and the supernatant was collected to calculate the copper concentration at specific time intervals.

2.6. Cell culture

The human cell lines 143B and U2OS were purchased from FuHeng Cell Center (Shanghai, China). The cells were cultured in a DMEM medium, containing 10% FBS, 100 units/mL penicillin, and 100 μg/mL streptomycin. The medium was changed every two days and cells were digested with trypsin/EDTA when cells reached 80%–90% confluence. Then cell suspension was centrifuged at 1000 rpm at room temperature for 5 min and used for experiments.

2.7. Cell viability

Briefly, cells were seeded into 96 well plates (3000 cells/well) overnight for cell attachment. Then, different concentrations of MSN and MCD (ranging from 0 to 250 μg/mL) were added to the culture medium. The plates were exposed to a 1064 nm laser (1 W/cm^2) for 5 min and continued to culture for 24 and 72 h. After 24 h and 72 h, added with CCK-8 solution according to the protocol (Dojindo Laboratories, Japan) for 2 h at 37 °C. Finally, the absorbance at 450 nm was assessed using a microplate reader.

The plates were exposed to a 1064 nm laser (1 W/cm^2) for 5 min and continued to culture for 24 and 72 h. Likewise, cells were stained by Calcein AM and PI to investigate cell survival.

2.8. Colony formation

Cells (143B and U2OS) were seeded into 6-well plates with a density of 800 cells/well. After material treatment and culture for 14 days, plates were washed with PBS three times and fixed with 4% paraformaldehyde for 30 min. Then cells were washed 3 times and stained with 1% crystal violet (Beyotime) for 20 min.

2.9. Cell migration and invasion

To determine the migration ability of 143B and U2OS cells, 1×10^5 cells were suspended in 100 μL serum-free high glucose medium and added into the upper chambers (8 μm, Corning), which were pre-coated with Matrigel (BD). Then the chambers were put into 600 μL DMEM (containing 10% FBS) for 24 h or 48 h. Finally, the chambers were fixed with 4% paraformaldehyde for 20 min and stained with crystal violet. Transmembrane cells were captured by microscope and calculated with ImageJ software.

2.10. Apoptosis and cell cycle

The cell apoptosis and cell cycle experiments were analyzed by flow cytometry. Cells were seeded into 6-well cell plates at a density of 1.0×10^6 cells per well. After 24 h of culture with different treatment, apoptosis rates were detected using an apoptosis detection kit (yeasen, China).

2.11. RNA extraction and quantitative real-time PCR analysis

Total RNA was extracted by using a TRIzol reagent according to the manufacturer's protocol. The remaining RNA was stored at −80 °C. RNA was reversed to cDNA via a HiFiScript cDNA kit (CWBIO). RT-PCR was performed with UltraSYBR Mixture (yeasen) by an ABI 7500 Sequencing Detection System (Applied Biosystems, Foster City, CA, USA). Specifically, an amplification reaction contains 1 μg cDNA and 1 μL primer

(0.5 μL forward primer and 0.5 μL reverse primer). The reaction condition was as follows: 40 cycles of denaturation at 95 °C for 10 s and amplification at 60 °C for 30 s. The primer pairs are shown in Table 1.

2.12. Western blot assay

Briefly, cells were lysed by radioimmunoprecipitation assay (RIPA) lysis buffer with phenylmethanesulfonylfluoride (PMSF, 1:100) for 20min at 4 °C and centrifuged at 1000 rpm for 10 min to collect the supernatant. Then, protein concentration was quantified by a bicinchoninic acid (BCA) kit, analyzed and separated in SDS-PAGE gels, and transferred onto a polyvinylidene fluoride (PVDF) membrane. The membrane was blocked with 5% BSA for 2 h at room temperature, 4 °C overnight, including GAPDH (1:1000), DALT (1:500), and FDX1(1:800), at 4 °C overnight. Finally, the membranes were incubated with a secondary antibody (1:2000, protein tech, China) for 2 h at room temperature and were exposed to a chemiluminescence system (Bio-Rad, USA) with ECL.

2.13. Anti-tumor in vivo

All animals and procedures were approved by the Zhejiang University Institutional Animal Care and Use Committee. OS animal model was constructed as previously described. Briefly, 1.0×10^7 luciferase-labeled 143B cells were injected into nude mice (6 weeks) and mice were kept for 2 weeks for tumor growth. Then, tumor tissue was harvested and cut into a tumor mass with a diameter of 2–3 mm, which was seeded into nude mice's proximal tibia. Nearly 10 days after model construction, the tumor size reached 50.0 mm^3, and mice were divided into six groups randomly (n = 5): (1) PBS, (2) MSN, (3) Cu_2S, (4) Cu_2S + NIR-II, (5) MCD, (6) MCD + NIR-II. 100 μL (10 mg/kg) material solution was injected into the caudal vein of nude mice. After injection 24 h, the tumor was irradiated with a 1064 nm NIR laser light (1 W/cm^2) for 5 min. After 10 cycles of treatment, the mice were euthanized, and the tumor was weighed and collected for subsequent histological examination. In addition, mice tibiae were collected for micro-CT analyses and histological examination. Heart, liver, spleen, and kidney tissues were collected to evaluate visceral tissue toxicity by H&E staining.

2.14. Anti-metastasis effect

Anti-metastasis effect was investigated by using the orthotopic spontaneous metastasis osteosarcoma model. D-luciferin (200 mg/kg, Meilune) was intraperitoneally injected into the anesthetized mice. After execution, the lung tissues of mice were visualized under a live imager and collected for histological examination.

2.15. Statistical analysis

All data were expressed as the mean ± SEM of three independent experiments at least. The results were analyzed by using Prism 8 version 5.0 (GraphPad Software) for Windows and A one-way ANOVA was used for the intergroup comparisons, followed by a Tukey test, and $p < 0.5$ was considered statistically significant.

Table 1
Primers used in RT-PCR.

Gene	Forward Primer	Reverse Primer
GAPDH	AGGTCGGTGTGAACGGATTTG	GGGGTCGTTGATGGCAACA
β-actin	GTGACGTTGACATCCGTAAAGA	GCCGGACTCATCGTACTCC
OCN	CCCTGAGTCTGACAAAGCCT	GCGGTCTTCAAGCCATACTG
OPN	TGGAGAGGTAGAAAAGGCACA	CAAACACACTCTTGGCACCAC
Runx2	GACTGTGGTTACCGTCATGGC	ACTTGGTTTTTCATAACAGCGGA
ALP	TTCATAAGCAGGCGGGGGA	GGTGTACCCTGAGATTCGTCC
BMP-2	GGGACCCGCTGTCTTCTAGT	TCAACTCAAATTCGCTGAGGAC
CTSK	TCCGCAATCCTTACCGAATA	AACTTGAACACCCACATCCTG
c-Fos	GTTCGTGAAACACACCAGGC	GGCCTTGACTCACATGCTCT
NFATc1	GGGTCAGTGTGACCGAAGAT	GGAAGTCAGAAGTGGGTGGA
DC-STAMP	GCTGTATCGGCTCATCTCCT	AAGGCAGAATCATGGACGAC

3. Results and discussion

3.1. Synthesis and characterization of the MCD

Cuproptosis is a novel form of programmed cell death that shows potential for cancer and tumor treatment. In this study, we synthesized GSH/pH responsive MCD nanoparticles for both tumor treatment and bone mineralization. The Cu_2S nanoparticles were 5.95 ± 0.83 nm in size, as seen in the transmission electron microscopy (TEM) image (Fig. 1A and S1A). The XPS spectrum of copper exhibited peaks at 952.9 eV and 932.9 eV corresponding to Cu^+ 2p3/2 and Cu^+ 2p1/2, respectively, indicating the formation of Cu_2S nanoparticles (Fig. 1B) [20,21]. The ultraviolet–visible absorption spectrum (Fig. 1C) showed a longitudinal plasmon peak at 1064 nm, suggesting that the Cu_2S nanoparticles have a suitable wavelength for mild photothermal therapy in the NIR-II range. The TEM image of the MSN nanospheres (Fig. 1D) revealed a dendritic mesoporous structure. The nitrogen adsorption/-desorption isotherms of the MSN nanospheres showed a type IV isotherm, confirming their porous nature. This was further supported by the precise isothermal curves observed (Fig. S1B). The pore volume of the MSN sample was determined to be 11.90 nm, indicating the high porosity of these nanospheres (Fig. 1E). After being coated with oxidized dextran, the MSN@oxidized dextran (MD) nanoparticles exhibited similar morphology to the MSN nanoparticles (Fig. 1F). TEM and corresponding element mapping results confirmed the successful loading of Cu_2S onto the MD nanoparticles, as evidenced by the presence of Si, O, S, and Cu elements (Fig. 1G). The zeta potential (z-potential) measurements (Fig. 1H) showed that the z-potential of the MSN and MSN-NH_2 nanoparticles were −23.6 mV and 16.8 mV, respectively, indicating the successful amino modification of MSN. The MSN-NH_2 carries a positive charge, while Cu_2S carries a negative charge. Due to the electrostatic attraction, Cu_2S is successfully loaded onto MSN-NH_2. The z-potential of the MCD was −37.7 mV after coating with oDEX and Cu_2S, indicating the formation of the MCD nanoparticles. The FT-IR spectrum exhibited distinct peaks at 3283 cm^{-1} (O–H), 2958 cm^{-1} (C═O), 1650 cm^{-1} (C–N), and 1530 cm-^{1} (N–H), confirming the presence of organics in the synthesis of Cu_2S nanoparticles (Fig. S1C) [18]. The FT-IR spectrum of oDEX showed a peak at 1734 cm^{-1}, attributed to the aldehyde group (-CHO), indicating the successful oxidation process of dextran (Fig. 1I) [22]. The FT-IR spectrum of MSN displayed peaks at 1086 cm^{-1} and 800 cm^{-1}, characteristic of amorphous silica (Si–*O*–Si). Additionally, the presence of S–S and C–S bonds, acting as bridging structures of thioethers, was observed at 565 cm^{-1} and 694 cm^{-1} (Fig. 1J) [23]. After the application of oDEX coating, a new peak at 1634 cm^{-1} appeared in the MD sample, representing the Schiff base bond between the –NH_2 of MSN and the –CHO of oDEX (Fig. S1D) [24]. The Schiff base bond used in these materials is sensitive to acidity and reversible, allowing release Cu_2S nanoparticles. The absorption peaks at 565 cm^{-1} and 694 cm^{-1} in the MCD samples are attributed to the vibration of the S–S and C–S bonds, respectively, which are derived from the bridging structure of thioethers (Fig. 1J). Additionally, the absorption peaks at 1452 cm^{-1}, 1651 cm^{-1}, 3307 cm^{-1}, and 2924 cm^{-1} are related to the organic components of the Cu_2S sample. Importantly, the S–S bond and Schiff base bond in these samples are sensitive to acidic and reductive conditions, which promote the degradation of the MCD sample in tumor microenvironments [23,25]. Besides, we added MCD to ddH_2O, PBS, DMEM, and FBS separately to investigate the stability of the material. Fig. S1E represents the material added and left to stand for 6 h, while Fig. S1F depicts the material added and left to stand for 24 h. As our material is coated with oDEX on the outermost layer, it serves to seal the loaded Cu_2S and, simultaneously, modifies the material to prevent protein adsorption. It also demonstrates good stability. Therefore, we

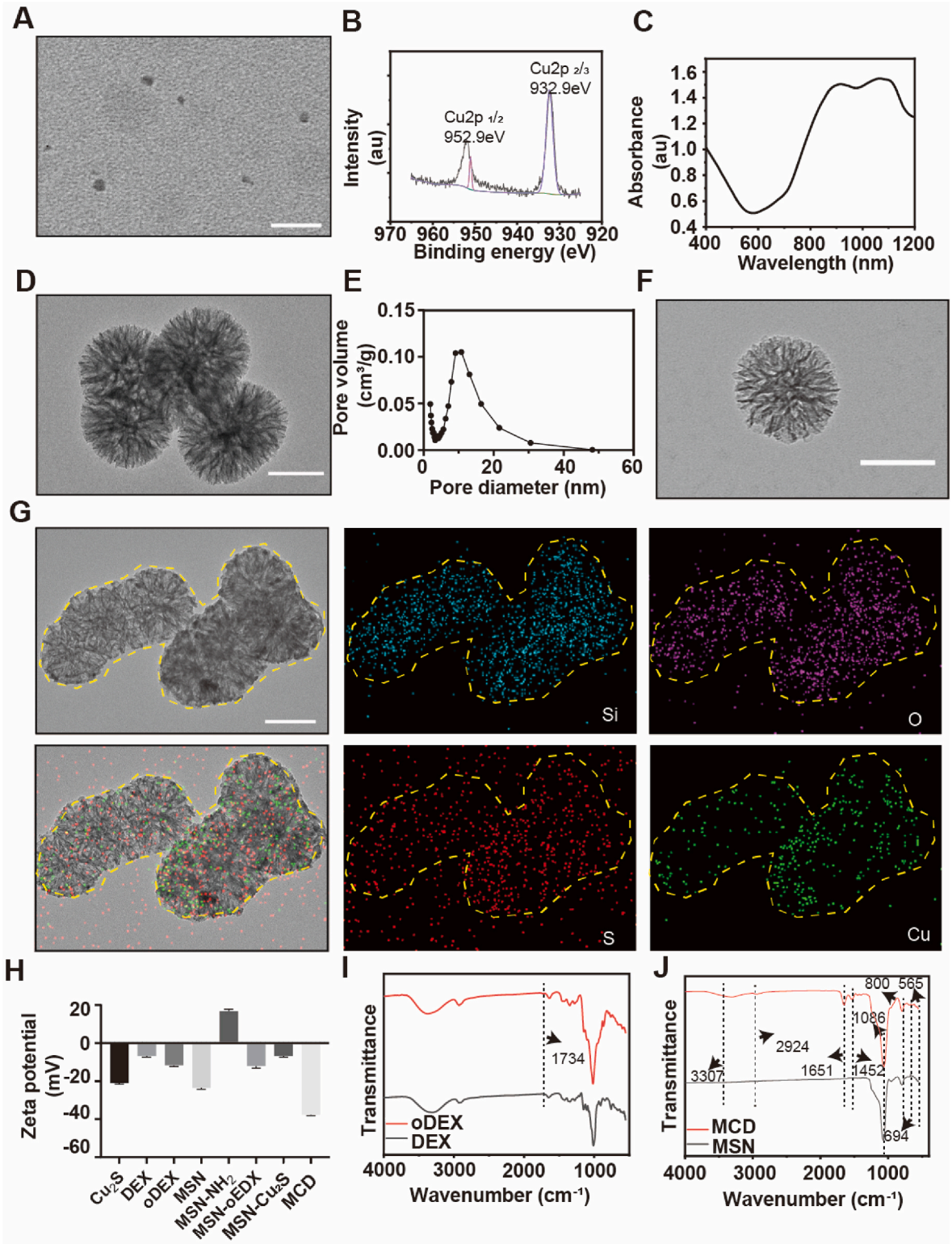

Fig. 1. Synthesis and characterizations of the MCD nanoparticles.
(A) TEM of the Cu_2S nanoparticles. Scale bar, 50 nm. (B) XPS spectra of the Cu_2S nanoparticles. (C) UV–vis spectra of the Cu_2S nanoparticles. (D) TEM image of the MSN. Scale bar, 100 nm. (E) Pore size distribution for the MSN. (F) TEM image of the MD. Scale bar, 100 nm. (G) Element mapping of the MCD nanoparticles. Scale bar, 100 nm. (H) The Zeta potential of the materials was assessed by a Zeta potential analyzer. (I–J) FT-IR spectra of the material.

successfully prepared MCD nanoparticles, but their functionality still needs further verification.

3.2. Sensibility and degradability of the MCD

The sensibility and degradability of MCD nanoparticles towards different pH levels and concentrations of GSH were assessed to

determine their suitability for use in a simulated tissue microenvironment. The degradability of the nanoparticles was found to not be influenced by the acidic level of the surrounding solvent without GSH. Analysis of the TEM image demonstrated that the nanoparticles without degradation, in an acidic microenvironment in the absence of GSH. Furthermore, the inclusion of GSH accelerated the degradation rate, indicating that the organic-inorganic MD nanoparticles exhibit pH and GSH sensitivity. This observation suggests that these nanoparticles have the potential to be used as tumor treatment agents (Fig. 2A). After exposure to pH = 6.5 and 10 mM GSH for 48 h, the MCD nanoparticles underwent near complete degradation, highlighting the impressive degradability of the materials.

The unique porous structure of MSN makes it an increasingly popular material for drug loading in medical applications [26]. Quantitative results indicate that under normal physiological conditions (pH = 7.4, GSH = 0 mM), the degradation rate is approximately 8.5% within 60 h, demonstrating the effective blocking capacity of the MCD nanoparticles (Fig. 2B). However, as the pH level decreases and the GSH concentration increases, the release rate of the nanoparticles significantly increases. For instance, after 60 h of culture, the cumulative release rates reach 16.7% at pH 6.5 and 23.2% at pH 6.0, respectively (Fig. 2C). This can be attributed to the breakdown of the Schiff base bond in an acidic environment, leading to an increase in the release of Cu_2S nanoparticles. At a pH of 7.4, the cumulative release rates for the Cu_2S nanoparticles with 0 mM GSH, 5 mM GSH, and 10 mM GSH are 8.5%, 43.4%, and 49.8%, respectively (Fig. 2B). However, under the same GSH conditions, as the pH decreases, the release rates increase to 16.7%, 47.4%, and 55.3% (Fig. 2D). This can be attributed to the S–S, S–C bond, and Schiff base bond of the materials. In conclusion, the organic-inorganic MCD nanoparticles exhibit a favorable degradation rate in low pH and high GSH concentration microenvironments, making them suitable for acidic tumor treatment. Otherwise, the released amounts of copper ions and hydrogen sulfide have been quantified.

Shreds of evidence have indicated that Cu_2S nanoparticles exhibit time-dependent photothermal behavior [27]. Fig. 1C also provides evidence that the Cu_2S nanoparticles have a common wavelength in the NIR-II range, making them suitable for mild photothermal therapy. To investigate their photothermal performance, the materials were subjected to irradiation with a 1064 nm NIR-II laser at power densities ranging from 0.5 to 2 W/cm^2, and the results are depicted in Fig. 2E. It can be observed that the temperatures of the PBS and MSN groups remained relatively stable during the continuous irrigation process over 5 min. In contrast, the photothermal performance of the MCD nanoparticles varied with an increase in the concentration of it. The quantitative analysis revealed that the temperatures of the MCD nanoparticles, treated with an irradiation laser for 5 min, were 40.1 ℃, 51.4 ℃, and 66.9 ℃ for concentrations of 62.5 μg/ml MCD, 125 μg/ml MCD, and 250 μg/ml MCD, respectively (Fig. 2F). Since a temperature of around 50 ℃ is deemed suitable for tumor cell destruction, the concentration of 125 μg/ml MCD nanoparticles was chosen for subsequent tumor treatment experiments. Additionally, Fig. 2G demonstrates that the temperature of the MCD nanoparticles increases with an elevation in the power density of the NIR-II laser. Therefore, a power density of 1 W/cm^2 was selected for the *in vitro* and *in vivo* anti-tumor tests. Moreover, the photothermal conversion efficiency of the MCD nanoparticles remained consistent during five repeated cycles, indicating their stability and suitability for periodic NIR-II irradiation treatment post-injection. Consequently, the MCD nanoparticles exhibit exceptional photothermal conversion performance with long-lasting stability, making them an ideal candidate for photothermal therapy. The material has been successfully prepared and can proceed to the next step of biological experiments.

3.3. The biocompatibility of the MCD for OS in vitro

The biocompatibility of the nanoparticles was assessed through CCK-8 and Live/Dead assays at different time points during the culturing process. The results of the CCK-8 assay indicated that the MSN nanospheres were non-toxic to 143B and U2OS tumor cells after 24 and 48 h of treatment. However, the MCD nanoparticles exhibited relatively high lethality towards 143B and U2OS cells compared to the MSN nanospheres. For instance, when treated with 125 μg/ml MCD nanoparticles for 48 h, the viability of 143B and U2OS cells was approximately 52.6% and 55.2%, respectively. Upon exposure to laser irradiation at 1 W/cm^2 for 5 min, the cell viability of 143B and U2OS decreased to only 30.3% and 31.6%, respectively, indicating the successful photothermal and anti-tumor capabilities of the MCD material (Fig. 3A). The Live/Dead images supported these findings, showing fusiform-like morphologies of 143B and U2OS cells in the control and MSN groups. However, the number of live cells in the MCD group was relatively low, and lease live cells were observed in the MCD + NIR-II group (Fig. 3B), which was consistent with the results obtained from the CCK-8 assays. Further quantitative analysis revealed that the viability of 143B cells after 24 h of treatment was 93.7%, 94.0%, 63.3%, and 26% in the Control, MSN, MCD, and MCD + NIR-II groups, respectively. Similarly, the MCD and MCD + NIR-II groups demonstrated effective reduction in the viability of U2OS cells, with values of approximately 66.3% and 33%, respectively, providing further evidence of the anti-tumor properties of the organic-inorganic MCD nanoparticles (Fig. 3C). Furthermore, the colony-forming assay confirmed the inhibitory effect of the materials and laser irradiation on 143B and U2OS cells (Fig. 3D). Quantitative analysis indicated that the area ratios of colonies for 143B cells in the control, MSN, MCD, and MCD + NIR-II groups were 56.7%, 52.4%, 29.1%, and 17.0%, respectively (Fig. 3E). In conclusion, these findings suggest that the organic-inorganic MCD nanoparticles possess excellent photothermal and anti-tumor properties, making them suitable for future tumor treatments. Therefore, it is necessary to proceed with the next step of mechanism exploration.

3.4. Underlying antitumor mechanism of the MCD nanoparticles

Tumor migration and invasion, which account for more than 90% of tumor-related deaths, are crucial functions that need to be investigated to understand the therapeutic mechanism of MCD nanoparticles [27,28]. To confirm the anti-metastatic ability of these nanoparticles, Transwell migration and invasion assays were conducted. The results, depicted in Fig. S2, show that the treatment of MCD nanoparticles led to a reduction in cell migration and invasion compared to the control and MSN groups, with even fewer cells observed after irradiation. These findings indicate that the pH/GSH-sensitive MCD nanoparticles, regardless of irradiation, could impact tumor survival and influence tumor migration and invasion.

The relationship between the cell cycle, cell apoptosis, and tumor cell metastasis has been well-established [29]. Consequently, controlling cell cycle arrest and apoptosis is crucial for regulating tumor cell growth and metastasis. To explore the potential therapeutic mechanism, the effects of pH/GSH-sensitive MCD nanoparticles on cell apoptosis and cell cycle were investigated (Figs. S3A–B). The results demonstrated that the MCD nanoparticles promoted apoptosis and cycle arrest in 143B and U2OS cells. Specifically, the MCD + NIR-II group induced tumor cell apoptosis and caused a proportionate increase in the G0/G1 phase for 143B cells and the S phase for U2OS cells.

To further understand the underlying mechanism of MCD for OS, we made a further attempt to reveal its action mechanism by RNA-Seq analysis. As shown in the volcano plot, 1025 downregulated genes and 618 upregulated genes were screened versus the control group (Fig. 4A). Comparing with the control group, various biological processes associated with cell cellular metal ion homeostasis, stress response to copper ion and stress response to copper ion were significantly changed, indicating that the treatment with MCD could remarkably disrupt intracellular copper homeostasis and inducing negative regulation of growth (Fig. 4B and C). Specifically, in the volcano plot map, microtubule-

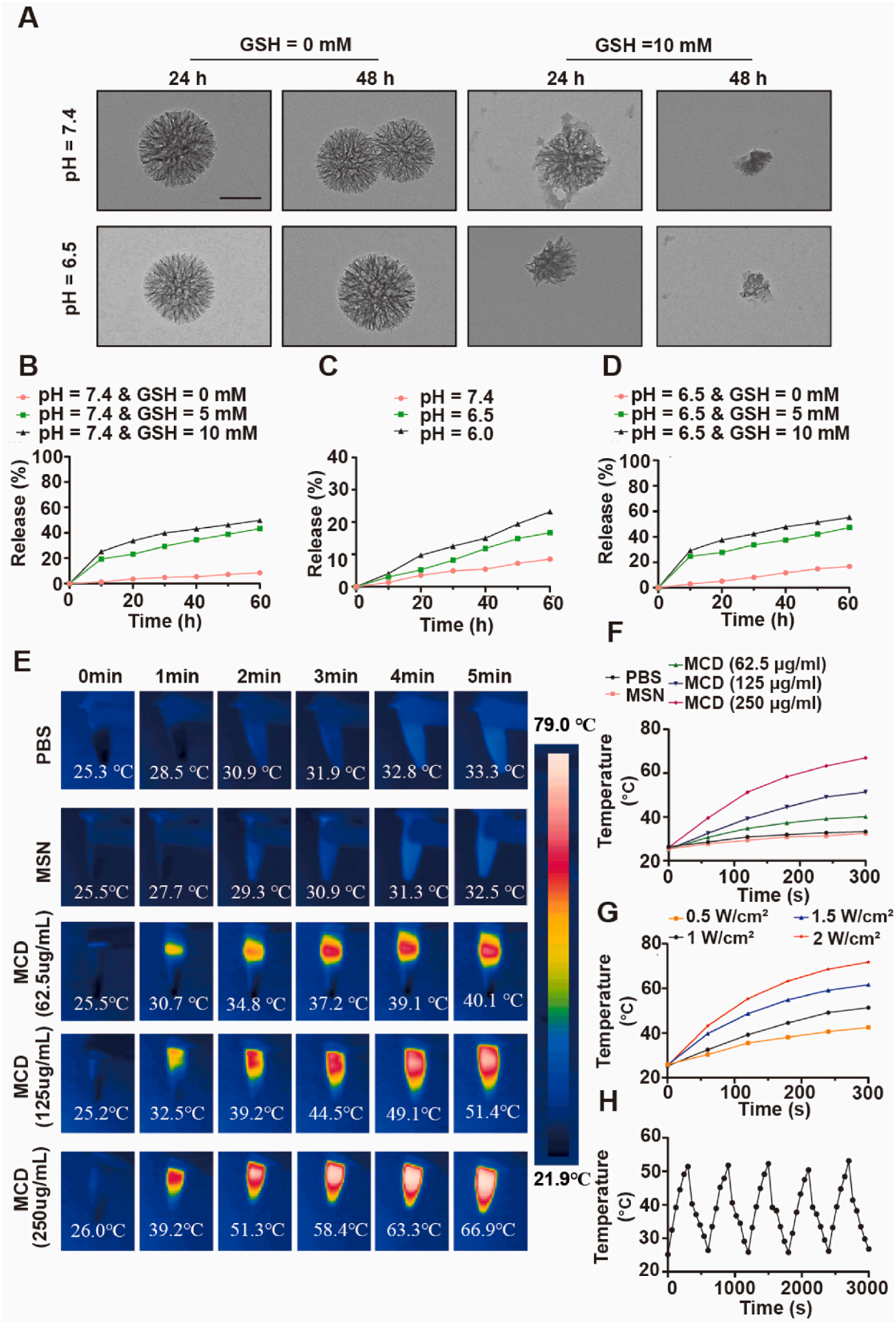

Fig. 2. Degradation, monitor release, and photothermal properties of the materials. (A) TEM images of the MD degraded in PBS at different pH values with or without 10 mM GSH. Scale bar, 50 nm. (B–D) The cumulative release of the Cu_2S nanoparticles from the MD in PBS at different pH values was treated with different concentrations of GSH. (E) Infrared thermographic maps of different materials with various concentrations after 5 min of NIR-II laser irradiation (1 W/cm^2). (F) Photothermal heating curves of different materials with various concentrations. (G) Temperature curves of the MCD nanoparticles treated with different power intensities. (H) Temperature variation of the MCD nanoparticles with 5 cycles of irradiation.

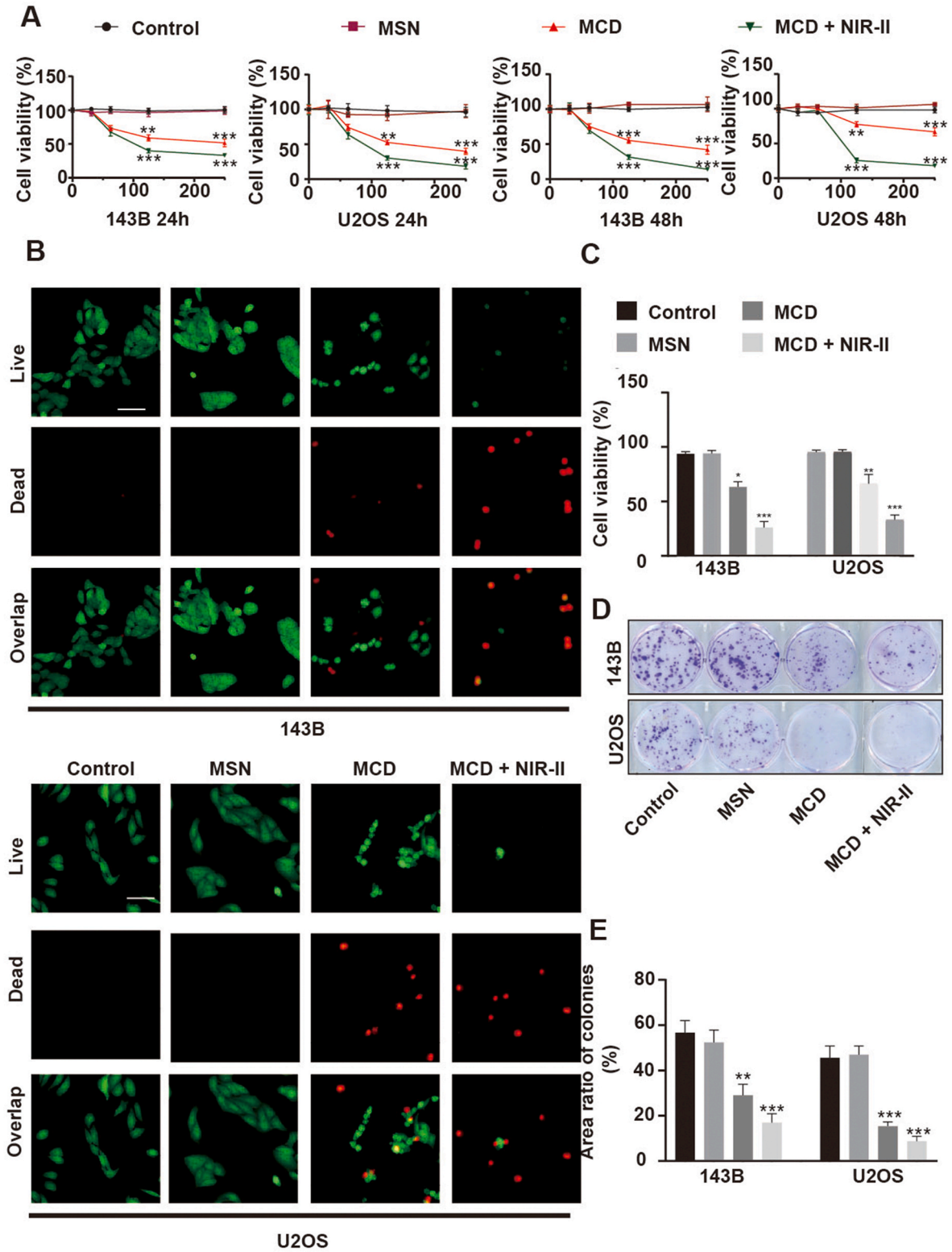

Fig. 3. Anti-tumor activity of the MCD nanoparticles *in vitro*. (A) Cytotoxic effect for 143B and U2OS cells of the MD and MCD nanoparticles with or without irradiation. The unit of concentration is μg/L. (B) Live/Dead fluorescence images for 143B and U2OS cells in each group. Scale bar: 50 μm. (C) Quantified results of Live/Dead staining. (D) Colony formation experiment of cells stained with crystal violet. (E) Quantitative results of the colony formation experiment. $^{*}P \leq 0.05$, $^{**}P \leq 0.01$, $^{***}P \leq 0.001$. (For interpretation of the references to color in this figure legend, the reader is referred to the Web version of this article.)

associated protein 1 light chain 3 alpha (MAP1LC3A), metallothionein 1E (MT1E) and solute carrier family 30 member 1 (SLC30A1) were up-regulated compared with control group, whose results were consistent with RT-PCR experiment (Fig. 4D). Copper toxicity is known to disrupt mitochondrial metabolism by interfering with key proteins involved in the tricarboxylic acid (TCA) cycle. The western blot (WB) analysis was conducted to investigate the effects of MCD nanoparticles on cuproptosis signaling pathways (Fig. 4E). Typically, copper ions are transported

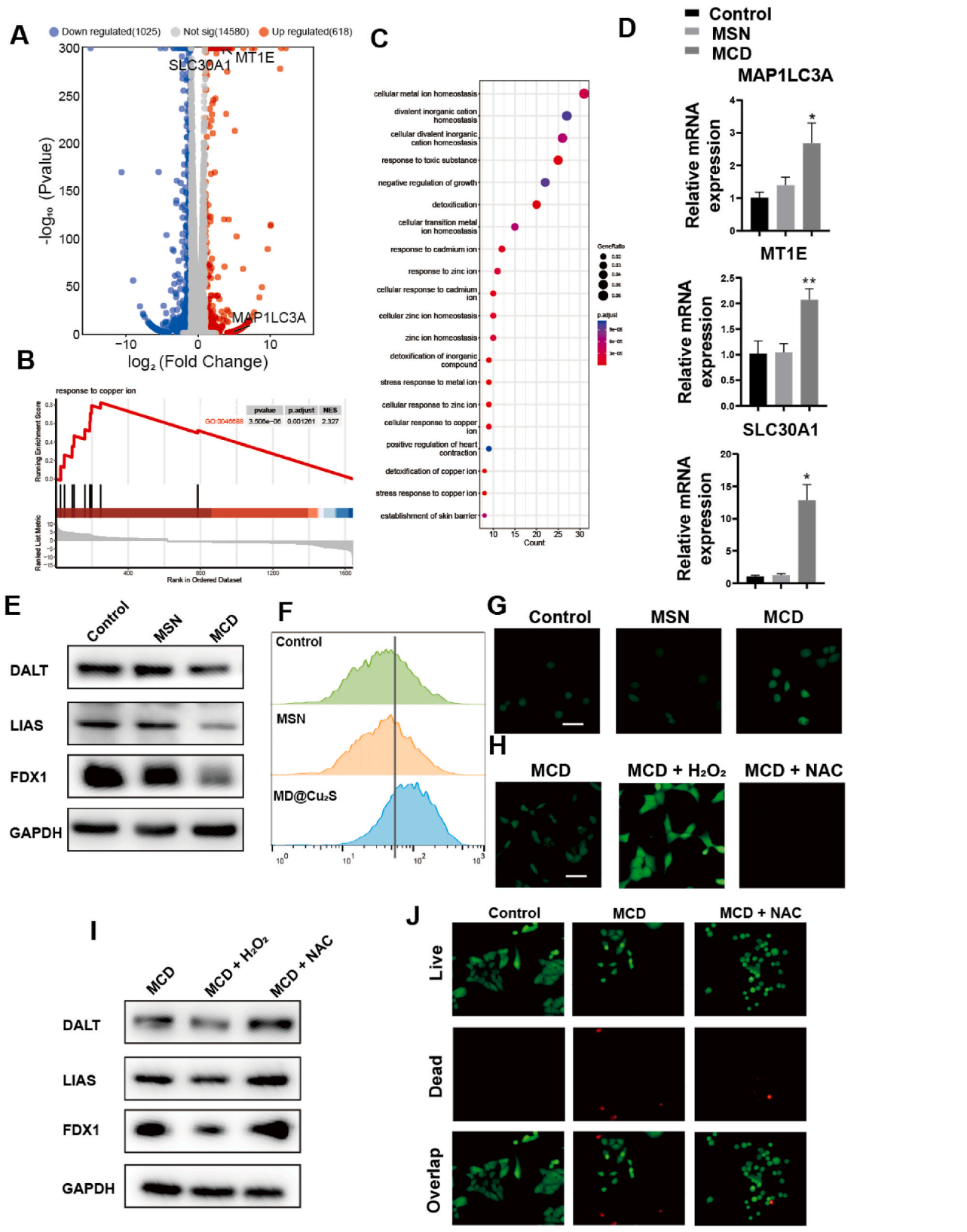

Fig. 4. Potential mechanism of the MCD nanoparticles for OS treatment. (A) Volcano plot of differentially expressed genes between control and MCD groups. (B) GSEA enrichment analysis of differentially expressed genes between control and MCD groups. (C) GO scatter plots of differentially expressed genes between control and MCD groups. (E) WB analyses of protein expressions in different groups. (F) Flow cytometry for ROS of cells with different treatments. (G, H) Fluorescence images of ROS in 143B cells with different treatments. Scale bar: 50 μm. (I) WB analyses of relative protein expressions in different groups. (J) Live/Dead fluorescence images for 143B and U2OS cells in each group. Scale bar: 50 μm $^{*}P \leq 0.05$, $^{**}P \leq 0.01$, $^{***}P \leq 0.001$.

across the mitochondrial membrane by elesclomol, a type of copper ionophore, and bind with dihydrolipoamide S-acetyltransferase (DLAT), a vital protein in the TCA cycle, resulting in DLAT aggregation. The expression of DLAT decreased upon treatment with MCD nanoparticles. Additionally, Ferredoxin 1 (FDX1), which transforms Cu^{2+} to Cu^{+}, was downregulated by the treatment. Cu^{+} can suppress lipoyl synthase (LIAS), an iron-sulfur (Fe–S) cluster protein, leading to the loss of the Fe–S cluster protein [30]. Overall, these findings suggest that MCD nanoparticles can inhibit the TCA process and induce cuproptosis. The western blot analysis for LIAS corroborated these expectations. Moreover, the results indicated a synergistic effect between ROS and cuproptosis. To evaluate the induction of ROS by pH/GSH-sensitive MCD nanoparticles, intracellular ROS levels were examined in 143B cells (Fig. 4F). The results showed an increase in ROS-positive green fluorescence in the MCD group compared to the other two groups. Acetylcysteine (NAC), a common ROS scavenger with direct and indirect antioxidant functions, was used to confirm the ROS induction [31]. Fluorescence images demonstrated that MCD nanoparticles induced ROS production in 143B cells (Fig. 4G). The addition of H_2O_2 resulted in a stronger fluorescent intensity compared to the MCD group, while the addition of NAC almost eliminated fluorescence, confirming the ROS-scavenging function of NAC and further validating the ROS induction by MCD nanoparticles (Fig. 4H). Additionally, the cuproptosis-related proteins were rescued by NAC and downregulated by H_2O_2 (Fig. 4I). These results were consistent with the fluorescence images, providing further evidence of the ROS induction by MCD nanoparticles (Fig. 4I). In this context, we investigated the role of removing ROS in the MCD and observed that the addition of NAC led to a reduction in the number of cells indicated by live/dead staining (Fig. 4J). This suggests a synergistic interaction between ROS and the material. Therefore, the experimental results demonstrate that MCD can promote cuproptosis in osteosarcoma cells, and ROS also plays a regulatory role in copper-induced cuproptosis -related protein.

3.5. The antibacterial capability of the MCD

There is growing evidence suggesting that the formation of tumors can lead to the presence of specific bacteria, which in turn can modify the tumor microenvironment [32,33]. Certain microorganisms, such as *E. coli* and *S. aureus*, have been found to promote tumor formation by creating an inflammatory environment conducive to tumor growth [34,35]. Therefore, targeting the microbiota is a promising strategy for the treatment of cancer. To evaluate the antibacterial performance of the materials, we assessed their ability to inhibit the growth of *E. coli* and *S. aureus* with and without the presence of the materials (Fig. S4). The results demonstrated that both the MCD and MCD + NIR-II groups exhibited antibacterial properties against *E. coli* and *S. aureus*. This suggests that the organic-inorganic biomaterials possess a strong broad-spectrum bactericidal activity, which can be attributed to the combined effects of the material itself and irradiation (Fig. S4).

3.6. Inhibition of osteoclast differentiation and function of the MCD

Osteoclasts, which originate from the monocyte lineage, are responsible for bone resorption *in vivo* [36]. The balance between bone formation and bone resorption is crucial for maintaining bone homeostasis. Abnormal activity of osteoclasts can lead to bone destruction in conditions such as periodontitis, osteoporosis, and osteosarcoma (OS) [37–39]. The interaction between osteoclasts and OS can create a vicious cycle that promotes osteosarcoma growth and osteolysis. Therefore, an ideal therapeutic drug for OS should not only kill tumor cells but also inhibit the formation and activity of osteoclasts. In this study, the inhibitory effect of MCD nanoparticles on osteoclasts was investigated by evaluating related osteoclastic factors (Fig. 5). The cytocompatibility and proliferation behavior of the biomaterials were assessed using CCK-8 assays and Live/Dead images. The results showed that MCD nanoparticles had no toxicity effect compared to the control and MSN groups after 24 and 72 h of treatment (Fig. 5A). Live/Dead images also revealed that bone marrow macrophages (BMMs) exhibited a spindle-like morphology in all groups, and quantitative results confirmed the good cytocompatibility of MCD biomaterials (Fig. 5B and C). The microenvironment of normal cells is neutral, and the expression of glutathione (GSH) is relatively low. Thus, the material shows comparatively lower release. MCD does not cause harm to BMMs. To further investigate the inhibitory effect of MCD nanoparticles on osteoclasts, the expression levels of c-Fos, DC-STAMP, NFATc1, and CTSK in BMMs were analyzed using real-time quantitative reverse transcription polymerase chain reaction (RT-PCR) (Fig. 5D). The results showed that the expression levels of these osteoclastic factors were relatively lower in the MCD + NIR-II group compared to the MCD, MSN, and control groups, indicating the inhibitory effect of MCD nanoparticles on BMMs' osteoclastic activity. In addition, TRAP staining was performed to assess osteoclast differentiation. The results showed that RANKL-treated BMMs in the MCD + NIR-II group had smaller cell sizes compared to the other three groups after 5 days of treatment (Fig. 5E and F). The area ratio of multinuclear osteoclast cells was consistent with the $TRAP^{+}$ cell numbers, indicating that MCD nanoparticles could influence mononuclear osteoclast cell fusion, which is a crucial step in osteoclast differentiation. Furthermore, the MCD + NIR-II group exhibited severe impairment of the RANKL-induced F-actin ring, which is necessary for mature osteoclast function in bone resorption (Fig. 5G and H) [40]. The actin belt numbers were significantly lower in the MCD + NIR-II group compared to the other groups, indicating the superior inhibitory effect of MCD material combined with irradiation. Moreover, bone resorption results demonstrated that the bone resorption ratio was lower in the MCD + NIR-II group and higher in the MSN groups compared to the control group (Fig. 5I and J). Similarly, the MCD nanoparticles disrupted the TCA process of BMMs, which obstructed osteoclast formation and maturation (Fig. 5K).

To mimic the interaction between tumor cells and osteoclasts in the OS microenvironment, 143B cells were co-cultured with Osteoclastic condition medium (Fig. 5L). The expression levels of osteoclast-related genes in BMMs with 143B cells were much lower in the MCD + NIR-II group compared to the other three groups (Figs. S5B–C). These findings suggest that the combined effect of MCD nanoparticles and irradiation can suppress osteoclast differentiation and function, as well as alter the expression of cuproptosis-related genes, leading to energy metabolism disorder.

3.7. Mechanism of inhibitory effect of materials on osteoclasts

In our study, we aimed to investigate how a certain material inhibits the activity of osteoclasts, by examining the involvement of reactive oxygen species (ROS) and cell cuproptosis. Fig. 6A illustrates that MCD led to an increase in ROS production in bone marrow-derived macrophages (BMMs), which was subsequently reversed by N-acetyl cysteine (NAC) treatment. It is important to note that the activation of osteoclast differentiation by RANKL is known to promote the production of ROS, thus contributing to osteoclastogenesis [41]. Surprisingly, when we suppressed the MCD-induced ROS production with NAC, the expression of osteoclast marker genes was found to be upregulated (Fig. 6B). These findings were further supported by TRAP staining results (Fig. 6C and D).

Furthermore, we observed that NAC inhibited the synergistic effect of ROS and copper-induced cell death in the mitochondria, resulting in the upregulation of tricarboxylic acid (TCA)-associated proteins. This rescue of MCD-induced mitochondrial energy disorder in osteoclasts explains the observed phenomenon (Fig. 6E).

In summary, our study demonstrates that the MCD material exerts an inhibitory effect on osteoclast activity by modulating ROS and cell cuproptosis. These findings provide crucial insights into the inhibitory mechanism of MCD material and offer valuable references for the

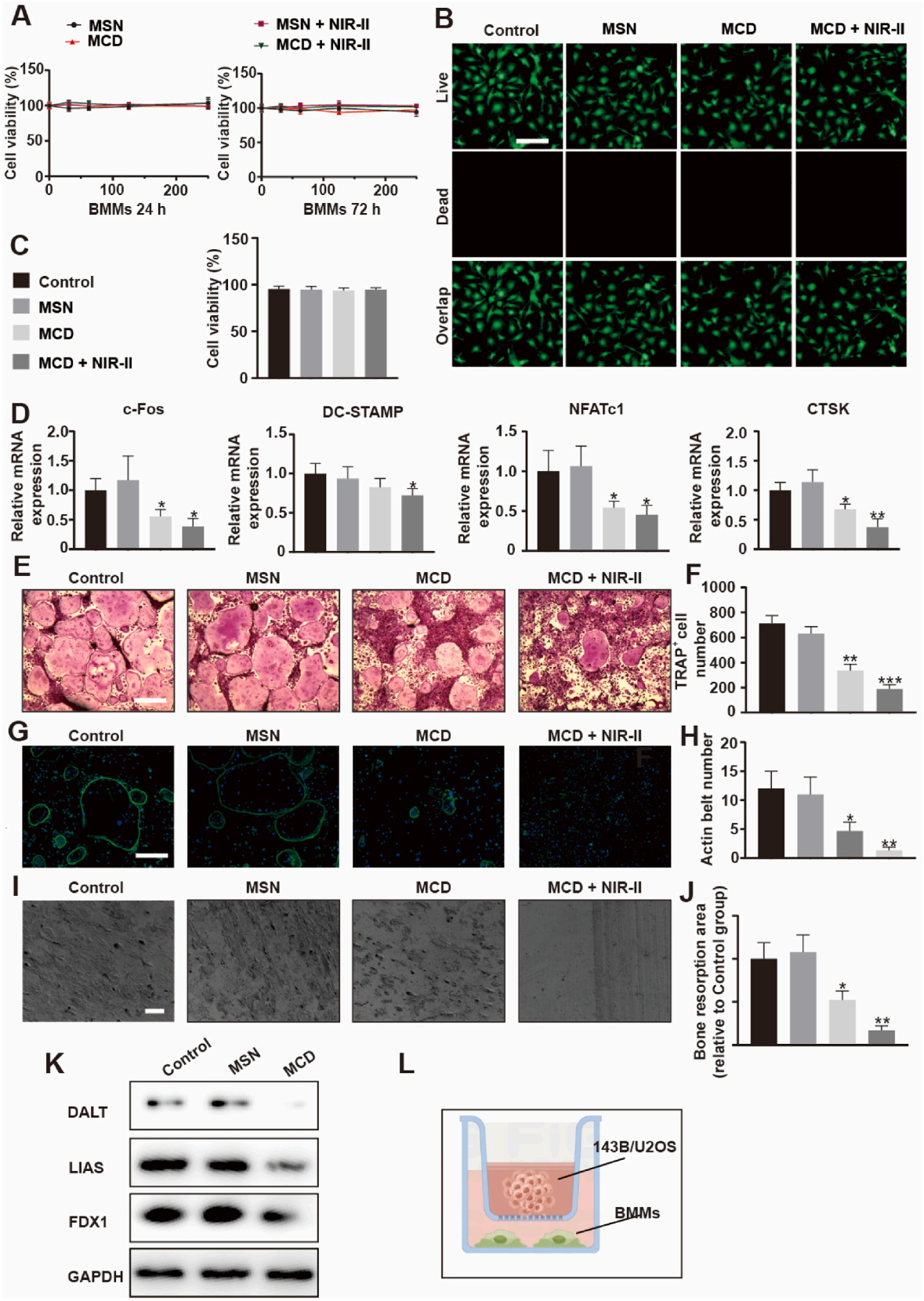

Fig. 5. Treatment for osteoclast *in vitro*. (A) CCK-8 assay for BMMs treated with different concentrations of the MSN and MCD nanoparticles with or without irradiation after 24 h or 72 h culture. The unit of concentration is μg/L. (B) Live/Dead fluorescence images of BMMs. Scale bar, 200 μm. (C) Statistical analyses of Live/Dead experiments. (D) Expression of osteoclast marker genes, including c-Fos, CTSK, NFATc1, and DC-STAMP. (E) Osteoclasts stained for TRAP. Scale bar, 500 μm. (F) TRAP staining, number, and size of the $TRAP^{+}$ osteoclasts with > 5 nuclei were quantified. (G–H) F-actin staining for osteoclast and F-actin analysis. Scale bar, 200 μm. (I–J) Bone resorption experiment and analysis. Scale bar, 200 μm. (K) WB analysis of relative protein expressions in different groups. (L) Schematic diagram of co-culture of BMMs with 143B and U2OS. $^{*}P \leq 0.05$, $^{**}P \leq 0.01$, $^{***}P \leq 0.001$.

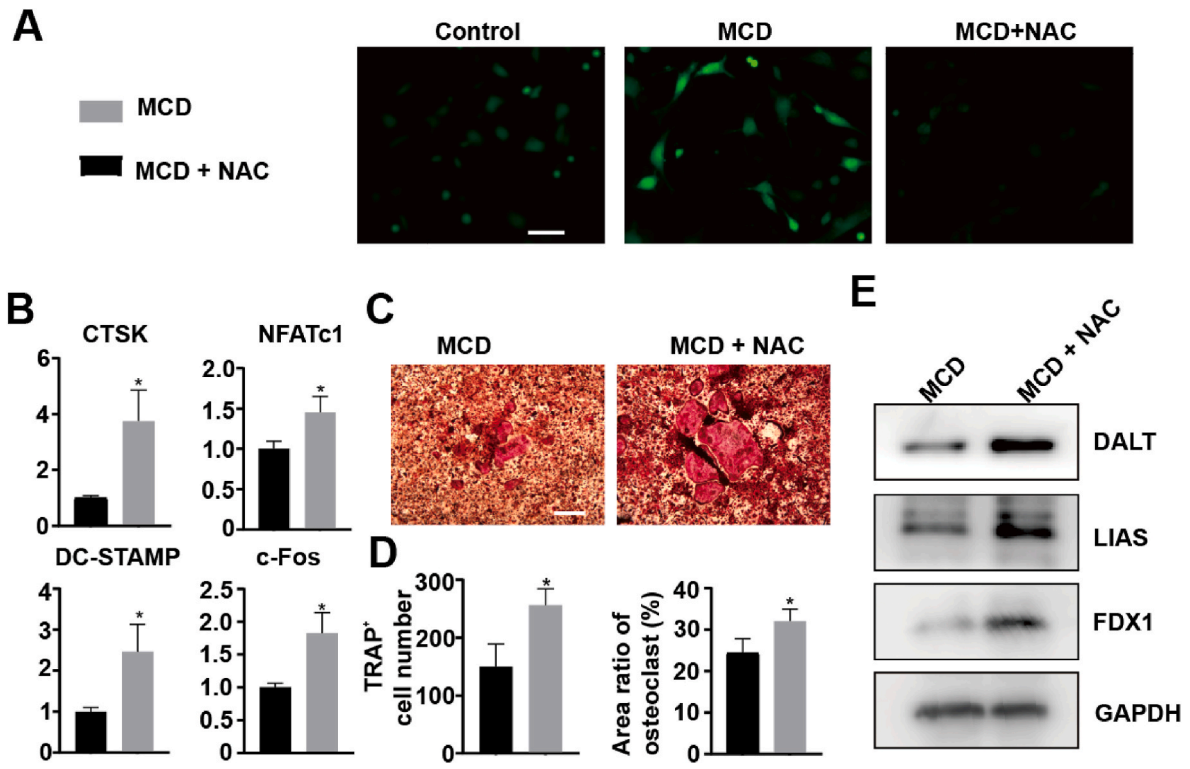

Fig. 6. Mechanism of inhibitory effect of materials on osteoclasts. (A) Flow cytometry for ROS of cells with different treatments. BMMs were treated with or without 125 μg/mL MCD with 6 h for cytophagy and washed by PBS. final culture with osteoclastogenic induction medium for 2 h. (B) Expression of osteoclast marker genes, including c-Fos, CTSK, NFATc1, and DC-STAMP. (C, D) TRAP staining, number, and size of the $TRAP^+$ osteoclasts with > 5 nuclei were quantified. (E) WB analyses of protein expressions in different groups. $^*P \leq 0.05$, $^{**}P \leq 0.01$, $^{***}P \leq 0.001$.

development of novel therapeutic approaches and materials.

3.8. Promotion of osteogenic differentiation and mineralization of the MCD

Trace ions play a crucial role in vertebrates and have been shown to improve bone repair by promoting osteogenesis [42–44]. Copper ions are essential in the proper regeneration and maturation of bone tissue [45]. However, osteosarcoma (OS), which includes primary bone tumors and metastatic bone tumors, causes severe tissue damage by inducing bone destruction and inhibiting bone repair [46,47]. To investigate the osteoinductivity of MCD nanoparticles, we subjected them to mild hyperthermia (around 40–42 °C) through irradiation. Initial tests using the CCK-8 assay showed that both the biomaterials and hyperthermia irradiation did not exhibit toxicity to bone marrow mesenchymal stem cells (BMSCs) (Fig. S6A). Further assessment using Live/Dead staining revealed that the presence of the biomaterials did not cause obvious cell death in BMSCs (Figs. S6B–C).

To evaluate the bone regeneration capabilities, we examined the osteogenic differentiation and mineralization of BMCs using alkaline phosphatase (ALP), Alizarin Red S (ARS), and RT-PCR assays. The RT-PCR results of ALP, OPN, RUNX2, OCN, and BMP2 in the MCD + NIR-II group were the highest among the four groups after 7 and 14 days of osteogenic culture (Figs. S6D–E). Similarly, the ALP and ARS staining results demonstrated the superior osteogenic capabilities of the MCD + NIR-II group, surpassing the other groups (Figs. S6F–G). Quantitative analysis further revealed that the ALP activities of the control, MSN, MCD, and MCD + NIR-II groups were 34.1, 34.4, 56.1, and 68.6, respectively (Fig. S5D). After 21 days of culture, there were significantly fewer calcium nodules observed in the control group, indicating the excellent osteogenic differentiation and mineralization capabilities of the organic-inorganic biomaterials.

3.9. Therapeutic performance for OS and OS metastasis of the MCD + NIR-II in vivo

The results of the study showed that there was minimal hemolysis observed in blood cells treated with different concentrations of MCD, indicating the good hemocompatibility of the biomaterials (Figs. S7A–B). To confirm the therapeutic effects of the biomaterials and irradiation *in vivo*, luciferase-labeled 143B cells were implanted to create an orthotopic spontaneous metastasis OS model. The nude mice with tumors up to 50 mm^3 were randomly divided into 6 groups (n = 5): (1) PBS, (2) MSN, (3) Cu_2S, (4) Cu_2S + NIR-II, (5) MCD, and (6) MCD + NIR-II. The experimental procedure is illustrated in Fig. 7A, where the mice with tumors were exposed to a 1064 nm laser for 5 min, repeated in 10 cycles over 20 days. Photothermal results showed that the temperature of the MCD + NIR-II group remained consistently higher compared to the other two groups (Fig. 7B), which could be attributed to the relatively smaller size of Cu_2S nanoparticles and their quick metabolism *in vivo*. Specifically, the temperature of the MCD + NIR-II group after 5 min of irradiation was 51.3 ℃, while those of the Cu_2S + NIR-II and control + NIR-II groups increased to 39.5 ℃ and 34.8 ℃, respectively (Fig. 7C). The tumor volume and weight of the MCD + NIR-II group were significantly lower compared to the other five groups (Fig. 7D–F), indicating the effective tumor-suppressing capability of MCD + NIR-II. During the therapeutic period, there were no differences in body weight among the groups (Fig. S8A). Additionally, the materials and irradiation treatment did not cause significant visceral damage in the nude mice (Fig. S9). Blood routine and hepatorenal function tests showed results within normal limits for all groups (Fig. S10). Histological analyses using Hematoxylin-Eosin (H&E) and Ki67 staining demonstrated a significant reduction in tumor cells with the treatment of biomaterials. Quantitative results revealed that the Ki67 positive ratios of the control, MSN, Cu_2S, Cu_2S + NIR-II, MCD, and MCD + NIR-II groups were 68.3%, 65.7%, 42.7%, 49.3%, 33.7%, 18.7%, respectively (Fig. S8B). Similarly,

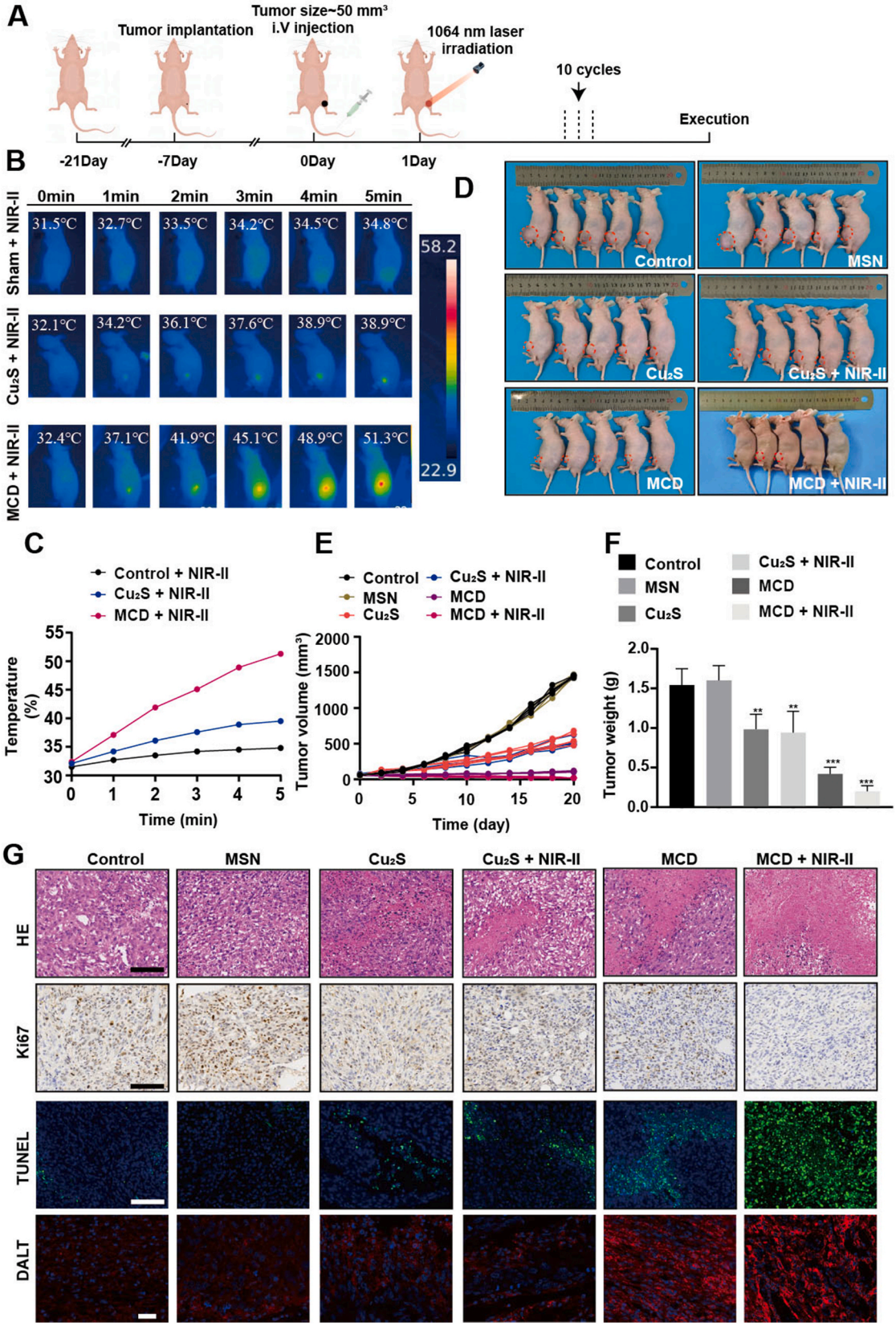

Fig. 7. Therapeutic performance for OS of the MCD + NIR-II *in vivo*. (A) Therapeutic procedure of OS model nude mice. (B) Infrared thermographic maps of temperature within 5 min in irradiated areas. (C) Time-dependent temperature curves in control, Cu_2S, and MCD groups *in vivo*. (D) Digital picture of OS model mice after 20 days of diverse treatments. (E) Tumor development curve. (F) Tumor weight. (G) H&E, TUNEL, IHC, and IFC staining. Scale bar, 100 μm $^*P \leq 0.05$, $^*P \leq 0.01$, $^*P \leq 0.001$.

TUNEL staining and quantitative results indicated that the MCD + NIR-II group had the highest tumor cell apoptosis and necrosis rate (Fig. 7H and S8C). Immunofluorescence staining was used to test the aggregation capability of lipoylated DLAT in all the groups, and it demonstrated a stronger DLAT aggregation ability in the MCD + NIR-II group (Fig. 7G). The most lethal disaster and clinical problem for patient survival rate in OS is lung metastases [48]. The anti-metastasis effect of the biomaterials was assessed using pulmonary bioluminescence imaging and H&E staining. In the experimental procedure, the mice received 10 treatment cycles over 20 days and were observed for 40 days (Fig. 8A). Survival results showed that OS lung metastases resulted in the death of almost all mice in both the control and MSN groups. The Cu_2S and MCD groups exhibited higher anti-metastasis abilities. Importantly, the introduction of laser irradiation further enhanced the capability of anti-OS lung metastasis in the MCD + NIR-II group, with a survival probability close to 100% (Fig. 8B). Bioluminescence images and H&E staining results further confirmed that the MCD + NIR-II group showed the best anti-metastasis capability (Fig. 8C and D). In summary, these findings indicate that MCD nanoparticles combined with irradiation effectively inhibit OS development and lung metastasis *in vivo* (insert a period here). Early metastasis and lung metastasis are frequently observed in osteosarcoma, constituting the primary cause of mortality in patients with this condition [49]. Therefore, suppressing pulmonary metastasis in osteosarcoma is a crucial approach to reduce the mortality rate in osteosarcoma patients. MCD can effectively inhibit the pulmonary metastasis of osteosarcoma, thereby improving the survival rate.

3.10. Therapeutic performance for tumor-associated osteolysis of the MCD + NIR-II in vivo

Previous experiments have demonstrated that the MCD + NIR-II group can inhibit osteoclast formation and promote osteoblast differentiation. Based on these findings, we hypothesized that the nanoparticles could potentially repair bone destruction caused by osteosarcoma *in vivo*. To evaluate bone tissue damage and regression, we conducted micro-CT (μCT) and histological analyses.

Fig. 9A illustrates the tibiae in different groups. The control and MSN groups displayed significant bone defects, whereas the MCD and MCD + NIR-II groups showed relatively intact tibiae. In comparison to the control group, the MCD + NIR-II group exhibited a 2.4-fold increase in bone volume (BV) and a 2.5-fold increase in the ratio of bone volume to total volume (BV/TV) (Fig. 9B and C). Histological analysis using H&E staining revealed the presence of a large number of tumor cells in the tibial plateau and canal of the control and MSN groups, while the other four groups showed minimal tumor cell presence (Fig. 9D). Remarkably, the treatment with MCD + NIR-II preserved the integrity of cortical and trabecular bone, which were severely damaged in the other groups.

Furthermore, we performed tartrate-resistant acid phosphatase (TRAP) staining to assess osteoclast formation and osteosarcoma-induced osteoclast differentiation in the tibial plateaus of nude mice (Fig. 9D). The results demonstrated the inhibitory effects of MCD + NIR-II on osteoclast formation. These findings suggest that the organic-inorganic MCD nanoparticles have potential applications in tumor treatment, containment of lung metastasis, and bone regeneration. They may serve as an ideal material for eliminating osteosarcoma and promoting biomineralization in a combinatory approach. The osteolytic destruction caused by osteosarcoma is a well-known complication [50]. Thus, prevention of osteolytic destruction is a major obstacle to enhancing the satisfaction of osteosarcoma patients. In this study, MCD demonstrated excellent function of therapeutic performance for tumor-associated osteolysis.

4. Conclusion

In summary, the organic-inorganic pH/GSH-sensitive MCD nanoparticles have been developed for antibacterial purposes, effective tumor blockade, and suppression of bone destruction. In osteosarcoma (OS), MCD impacts proteins such as DALT and LIAS, thereby influencing the TCA cycle and leading to cell death through cuproptosis. Additionally, the material generates ROS, which further contributes to this

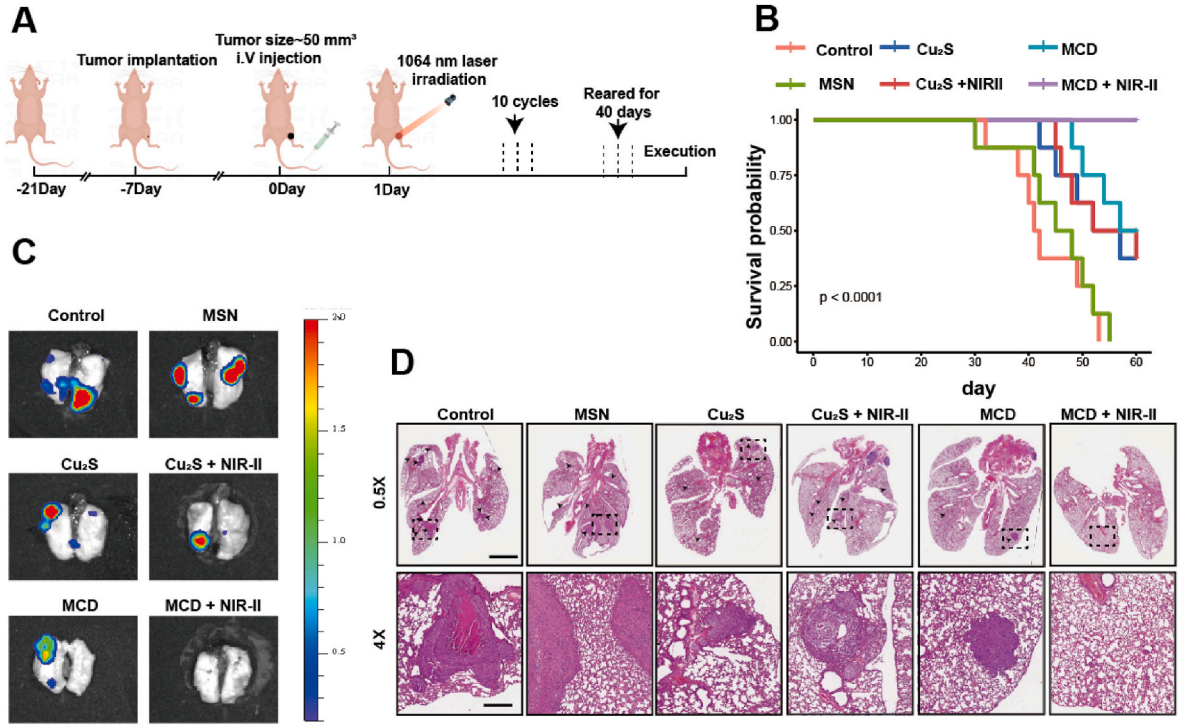

Fig. 8. Therapeutic performance for OS metastasis of the MCD + NIR-II *in vivo*. (A) Therapeutic procedure of OS metastasis model nude mice. (B) OS model survival curves. (C) Representative lung bioluminescence images from nude mice. (D) H&E staining for the lung of each group. Black arrows suggest lung metastases: scale bars, 2 mm (0.5×) and 250 μm (4×).

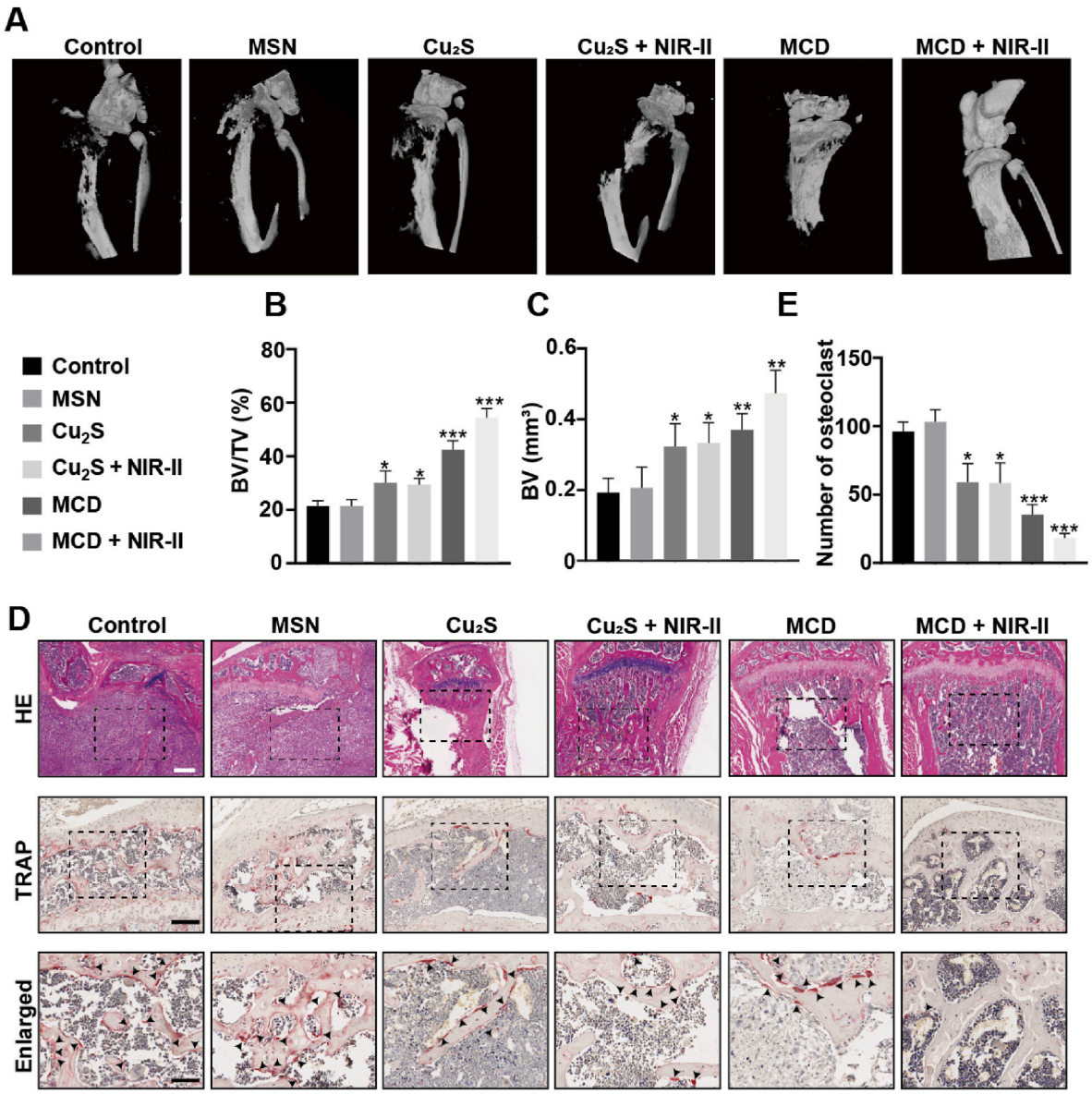

Fig. 9. Bone protection and osteoclast inhibition by the MCD + NIR-II. (A) μCT scanning of the left tibiae from control, MSN, 10 mg/kg Cu_2S, and 10 mg/kg MCD groups with or without irradiation. (B–C) Statical analyses of bone microstructural parameters: BV/TV and BV. (D) H&E and TRAP were staining for tibial sections from six groups. Black arrows suggest osteoclast. Scale bars, 250 μm (top image), 100 μm (middle image), and 50 μm (bottom image). (E) Number of $TRAP^+$ osteoclasts analyzed by TRAP staining. $^*P \leq 0.05$, $^*P \leq 0.01$, $^*P \leq 0.001$.

process. Furthermore, MCD has been found to promote tumor cell death through mild photothermal therapy and H_2S. In the case of osteoclasts, MCD also inhibits the energy metabolism of osteoclast differentiation and function by affecting the TCA cycle. Therefore, our material effectively disrupts energy metabolism, leading to the inhibition of osteoclast differentiation and function, and offering a potential therapeutic approach for osteosarcoma.

However, in this study, we only utilized two osteosarcoma cell lines, 143B and U2OS, for cellular research. However, there are other osteosarcoma cell lines, such as HOS, which we did not investigate. Additionally, in the animal experiments, we exclusively used the 143B cell line for *in vivo* studies, although this cell line is commonly used in osteosarcoma research involving animal models. We did not use other osteosarcoma cell lines for *in vivo* experiments.

CRediT authorship contribution statement

Lin Ye: Conceptualization, Investigation, Methodology, Writing – original draft. **Congcong Yu:** Methodology, Validation, Writing – original draft. **Jiechao Xia:** Methodology, Validation. **Kainan Ni:** Visualization. **Yejin Zhang:** Supervision. **Xiaozhang Ying:** Investigation. **Dingqi Xie:** Validation. **Yang Jin:** Visualization. **Rongtai Sun:** Funding acquisition, Writing – original draft. **Ruikang Tang:** Funding acquisition, Writing – review & editing. **Shunwu Fan:** Conceptualization, Funding acquisition. **Shasha Yao:** Conceptualization, Funding acquisition, Writing – review & editing.

Declaration of competing interest

The authors declare that they have no known competing financial interests or personal relationships that could have appeared to influence the work reported in this paper.

Data availability

Data will be made available on request.

Acknowledgements

The study was supported by the National Natural Science Foundation of China (Grant No. 82002284), the Health Commission of Zhejiang Province (Grant No. 2021449373), the National Science and Technology Major Project (Grant Nos. 2020YFC1107100).

Appendix A. Supplementary data

Supplementary data to this article can be found online at https://doi.org/10.1016/j.mtbio.2024.100996.

References

[1] M. He, G. Wang, L. Jiang, C. Qiu, B. Li, J. Wang, Y. Fu, miR-486 suppresses the development of osteosarcoma by regulating PKC-delta pathway, Int. J. Oncol. 50 (5) (2017) 1590–1600.
[2] Z. Yang, J. Liu, Y. Lu, Doxorubicin and CD-CUR inclusion complex co-loaded in thermosensitive hydrogel PLGA-PEG-PLGA localized administration for osteosarcoma, Int. J. Oncol. 57 (2) (2020) 433–444.
[3] G. Ye, M. Huang, Y. Li, J. Ouyang, M. Chen, Q. Wen, X. Li, H. Zeng, P. Long, Z. Fan, J. Yin, W. Ye, D. Zhang, The FAP alpha -activated prodrug Z-GP-DAVLBH inhibits the growth and pulmonary metastasis of osteosarcoma cells by suppressing the AXL pathway, Acta Pharm. Sin. B 12 (3) (2022) 1288–1304.
[4] L. Huang, Z. Huang, W. Lin, L. Wang, X. Zhu, X. Chen, S. Yang, C. Lv, Salidroside suppresses the growth and invasion of human osteosarcoma cell lines MG63 and U2OS in vitro by inhibiting the JAK2/STAT3 signaling pathway, Int. J. Oncol. 54 (6) (2019) 1969–1980.
[5] S. Takagi, Y. Sasaki, S. Koike, A. Takemoto, Y. Seto, M. Haraguchi, T. Ukaji, T. Kawaguchi, M. Sugawara, M. Saito, Y. Funauchi, K. Ae, S. Matsumoto, N. Fujita, R. Katayama, Platelet-derived lysophosphatidic acid mediated LPAR1 activation as a therapeutic target for osteosarcoma metastasis, Oncogene 40 (36) (2021) 5548–5558.
[6] J. Yang, D. Cheng, S. Zhou, B. Zhu, T. Hu, Q. Yang, Overexpression of X-box binding protein 1 (XBP1) correlates to poor prognosis and up-regulation of PI3K/mTOR in human osteosarcoma, Int. J. Mol. Sci. 16 (12) (2015) 28635–28646.
[7] M. Tsuge, M. Osaki, R. Sasaki, M. Hirahata, F. Okada, SK-216, a novel inhibitor of plasminogen activator inhibitor-1, suppresses lung metastasis of human osteosarcoma, Int. J. Mol. Sci. 19 (3) (2018).
[8] B. Navet, K. Ando, J.W. Vargas-Franco, R. Brion, J. Amiaud, K. Mori, H. Yagita, C. G. Mueller, F. Verrecchia, C. Dumars, M.F. Heymann, D. Heymann, F. Lezot, The intrinsic and extrinsic implications of RANKL/RANK signaling in osteosarcoma: from tumor initiation to lung metastases, Cancers 10 (11) (2018).
[9] H. Kim, N. Takegahara, M.C. Walsh, S.A. Middleton, J. Yu, J. Shirakawa, J. Ueda, Y. Fujihara, M. Ikawa, M. Ishii, J. Kim, Y. Choi, IgSF11 regulates osteoclast differentiation through association with the scaffold protein PSD-95, Bone Res 8 (2020) 5.
[10] R. Dhandapani, P.D. Krishnan, A. Zennifer, V. Kannan, A. Manigandan, M.R. Arul, D. Jaiswal, A. Subramanian, S.G. Kumbar, S. Sethuraman, Additive manufacturing of biodegradable porous orthopaedic screw, Bioact. Mater. 5 (3) (2020) 458–467.
[11] P.C. Chen, C.H. Tang, L.W. Lin, C.H. Tsai, C.Y. Chu, T.H. Lin, Y.L. Huang, Thrombospondin-2 promotes prostate cancer bone metastasis by the up-regulation of matrix metalloproteinase-2 through down-regulating miR-376c expression, J. Hematol. Oncol. 10 (1) (2017) 33.
[12] P. Tsvetkov, S. Coy, B. Petrova, M. Dreishpoon, A. Verma, M. Abdusamad, J. Rossen, L. Joesch-Cohen, R. Humeidi, R.D. Spangler, J.K. Eaton, E. Frenkel, M. Kocak, S.M. Corsello, S. Lutsenko, N. Kanarek, S. Santagata, T.R. Golub, Copper induces cell death by targeting lipoylated TCA cycle proteins, Science 375 (6586) (2022) 1254–1261.
[13] M. Yang, H. Zheng, K. Xu, Q. Yuan, Y. Aihaiti, Y. Cai, P. Xu, A novel signature to guide osteosarcoma prognosis and immune microenvironment: cuproptosis-related lncRNA, Front. Immunol. 13 (2022).
[14] M. Li, Q. Song, Y. Bai, F. Hua, T. Wu, J. Liu, Comprehensive analysis of cuproptosis in immune response and prognosis of osteosarcoma, Front. Pharmacol. 13 (2022) 992431.
[15] T.A. Su, D.S. Shihadih, W. Cao, T.C. Detomasi, M.C. Heffern, S. Jia, A. Stahl, C. J. Chang, A modular ionophore platform for liver-directed copper supplementation in cells and animals, J. Am. Chem. Soc. 140 (42) (2018) 13764–13774.
[16] M. Sharma, R. Pandey, D. Saluja, ROS is the major player in regulating altered autophagy and lifespan in sin-3 mutants of C. elegans, Autophagy 14 (7) (2018) 1239–1255.
[17] C. Xu, Z. Yuan, N. Kohler, J. Kim, M.A. Chung, S. Sun, FePt nanoparticles as an Fe reservoir for controlled Fe release and tumor inhibition, J. Am. Chem. Soc. 131 (42) (2009) 15346–15351.
[18] A. Swaidan, S. Ghayyem, A. Barras, A. Addad, S. Szunerits, R. Boukherroub, Enhanced antibacterial activity of CuS-BSA/Lysozyme under near infrared light irradiation, Nanomaterials 11 (9) (2021).
[19] J.T. Lin, J.K. Du, Y.Q. Yang, L. Li, D.W. Zhang, C.L. Liang, J. Wang, J. Mei, G. H. Wang, pH and redox dual stimulate-responsive nanocarriers based on hyaluronic acid coated mesoporous silica for targeted drug delivery, Mater Sci Eng C Mater Biol Appl 81 (2017) 478–484.
[20] B. Ma, S. Wang, F. Liu, S. Zhang, J. Duan, Z. Li, Y. Kong, Y. Sang, H. Liu, W. Bu, L. Li, Self-assembled copper-amino acid nanoparticles for in situ glutathione "AND" H(2)O(2) sequentially triggered chemodynamic therapy, J. Am. Chem. Soc. 141 (2) (2019) 849–857.
[21] Y. Pei, J. Cheng, H. Zhong, Z. Pi, Y. Zhao, F. Jin, Sulfide-oxidation-assisted electrochemical water splitting for H2 production on a bifunctional Cu2S/nickel foam catalyst, Green Chem. 23 (18) (2021) 6975–6983.
[22] C. Wang, M. Wang, T. Xu, X. Zhang, C. Lin, W. Gao, H. Xu, B. Lei, C. Mao, Engineering bioactive self-healing antibacterial exosomes hydrogel for promoting chronic diabetic wound healing and complete skin regeneration, Theranostics 9 (1) (2019) 65–76.
[23] L. Zhang, L. Wang, H. Yao, F. Xu, Y. Chen, Biodegradable and biocompatible monodispersed hollow mesoporous organosilica with large pores for delivering biomacromolecules, J. Mater. Chem. B 5 (39) (2017) 8013–8025.
[24] J.W. Schafer, S.D. Schwartz, Directed evolution's influence on rapid density fluctuations illustrates how protein dynamics can become coupled to chemistry, ACS Catal. 10 (15) (2020) 8476–8484.
[25] X. Du, L. Xiong, S. Dai, F. Kleitz, S.Z. Qiao, Intracellular microenvironment-responsive dendrimer-like mesoporous nanohybrids for traceable, effective, and safe gene delivery, Adv. Funct. Mater. 24 (48) (2014) 7627–7637.
[26] S. Yang, X. Gao, Y. He, Y. Hu, B. Xu, Z. Cheng, M. Xiang, Y. Xie, Applying an innovative biodegradable self-assembly nanomicelles to deliver alpha-mangostin for improving anti-melanoma activity, Cell Death Dis. 10 (3) (2019) 146.
[27] B. Li, Z. Jiang, D. Xie, Y. Wang, X. Lao, Cetuximab-modified CuS nanoparticles integrating near-infrared-II-responsive photothermal therapy and anti-vessel treatment, Int. J. Nanomed. 13 (2018) 7289–7302.
[28] X. Zheng, W. Kang, H. Liu, S. Guo, Inhibition effects of total flavonoids from Scutellaria barbata D. Don on human breast carcinoma bone metastasis via downregulating PTHrP pathway, Int. J. Mol. Med. 41 (6) (2018) 3137–3146.
[29] J. Liu, M. Yang, W. Zhao, X. Zhou, CCPE: cell cycle pseudotime estimation for single cell RNA-seq data, Nucleic Acids Res. 50 (2) (2022) 704–716.
[30] J. Zhou, Q. Yu, J. Song, S. Li, X.L. Li, B.K. Kang, H.Y. Chen, J.J. Xu, Photothermally triggered copper payload release for cuproptosis-promoted cancer synergistic therapy, Angew Chem. Int. Ed. Engl. 62 (12) (2023) e202213922.
[31] K. Kalimeris, P. Briassoulis, A. Ntzouvani, T. Nomikos, K. Papaparaskeva, A. Politi, C. Batistaki, G. Kostopanagiotou, N-acetylcysteine ameliorates liver injury in a rat model of intestinal ischemia reperfusion, J. Surg. Res. 206 (2) (2016) 263–272.
[32] S. Choi, J. Chung, M.L. Cho, D. Park, S.S. Choi, Analysis of changes in microbiome compositions related to the prognosis of colorectal cancer patients based on tissue-derived 16S rRNA sequences, J. Transl. Med. 19 (1) (2021) 485.
[33] K.D. LaCourse, M. Zepeda-Rivera, A.G. Kempchinsky, A. Baryiames, S.S. Minot, C. D. Johnston, S. Bullman, The cancer chemotherapeutic 5-fluorouracil is a potent Fusobacterium nucleatum inhibitor and its activity is modified by intratumoral microbiota, Cell Rep. 41 (7) (2022) 111625.
[34] E.M. Park, M. Chelvanambi, N. Bhutiani, G. Kroemer, L. Zitvogel, J.A. Wargo, Targeting the gut and tumor microbiota in cancer, Nat. Med. 28 (4) (2022) 690–703.
[35] A. Lopes, E. Billard, A.H. Casse, R. Villeger, J. Veziant, G. Roche, G. Carrier, P. Sauvanet, A. Briat, F. Pages, S. Naimi, D. Pezet, N. Barnich, B. Dumas, M. Bonnet, Colibactin-positive Escherichia coli induce a procarcinogenic immune environment leading to immunotherapy resistance in colorectal cancer, Int. J. Cancer 146 (11) (2020) 3147–3159.
[36] X. Wei, Z. Zheng, Z. Feng, L. Zheng, S. Tao, B. Zheng, B. Huang, X. Zhang, J. Liu, Y. Chen, W. Zong, Z. Shan, S. Fan, J. Chen, F. Zhao, Sigma-1 receptor attenuates osteoclastogenesis by promoting ER-associated degradation of SERCA2, EMBO Mol. Med. 14 (7) (2022) e15373.
[37] J. Huang, C. Wu, B. Tian, X. Zhou, N. Ma, Y. Qian, Myricetin prevents alveolar bone loss in an experimental ovariectomized mouse model of periodontitis, Int. J. Mol. Sci. 17 (3) (2016) 422.
[38] L. Zhou, G. Hong, S. Li, Q. Liu, F. Song, J. Zhao, J. Yuan, J. Tickner, J. Xu, Fangchinoline protects against bone loss in OVX mice via inhibiting osteoclast formation, bone resorption and RANKL-induced signaling, Int. J. Biol. Sci. 16 (2) (2020) 309–319.
[39] L. Liu, H. Geng, C. Mei, L. Chen, Zoledronic acid enhanced the antitumor effect of cisplatin on orthotopic osteosarcoma by ROS-PI3K/AKT signaling and attenuated osteolysis, Oxid. Med. Cell. Longev. 2021 (2021) 6661534.
[40] J. Li, C. Deng, W. Liang, F. Kang, Y. Bai, B. Ma, C. Wu, S. Dong, Mn-containing bioceramics inhibit osteoclastogenesis and promote osteoporotic bone regeneration via scavenging ROS, Bioact. Mater. 6 (11) (2021) 3839–3850.
[41] Y. Xu, L.R. Morse, R.A.B. da Silva, D. Wang, R.A. Battaglino, A short report: PAMM, a novel antioxidant protein, induced by oxidative stress, Redox Biol. 6 (2015) 446–453.
[42] X. Qiao, J. Yang, Y. Shang, S. Deng, S. Yao, Z. Wang, Y. Guo, C. Peng, Magnesium-doped nanostructured titanium surface modulates macrophage-mediated inflammatory response for ameliorative osseointegration, Int. J. Nanomed. 15 (2020) 7185–7198.
[43] D. Xu, J. Qian, X. Guan, L. Ren, K. Yang, X. Huang, S. Zhang, Y. Chai, X. Wu, H. Wu, X. Zhang, K. Yang, B. Yu, Copper-containing alloy as immunoregulatory material in bone regeneration via mitochondrial oxidative stress, Front. Bioeng. Biotechnol. 8 (2020) 620629.
[44] I. Ortiz de Solorzano, M. Prieto, G. Mendoza, T. Alejo, S. Irusta, V. Sebastian, M. Arruebo, Microfluidic synthesis and biological evaluation of photothermal biodegradable copper sulfide nanoparticles, ACS Appl. Mater. Interfaces 8 (33) (2016) 21545–21554.

[45] S. Suvarnapathaki, X. Wu, T. Zhang, M.A. Nguyen, A.A. Goulopoulos, B. Wu, G. Camci-Unal, Oxygen generating scaffolds regenerate critical size bone defects, Bioact. Mater. 13 (2022) 64–81.
[46] E.P. McNeill, R.W. Reese, A. Tondon, B.H. Clough, S. Pan, J. Froese, D. Palmer, U. Krause, D.M. Loeb, R. Kaunas, C.A. Gregory, Three-dimensional in vitro modeling of malignant bone disease recapitulates experimentally accessible mechanisms of osteoinhibition, Cell Death Dis. 9 (12) (2018) 1161.
[47] D.J. Civitello, L.H. Baker, S. Maduraiveeran, R.B. Hartman, Resource fluctuations inhibit the reproduction and virulence of the human parasite Schistosoma mansoni in its snail intermediate host, Proc. Biol. Sci. 287 (1919) (2020) 20192446.
[48] Z. Wu, T. Han, H. Su, J. Xuan, X. Wang, Comprehensive analysis of fatty acid and lactate metabolism-related genes for prognosis value, immune infiltration, and therapy in osteosarcoma patients, Front. Oncol. 12 (2022) 934080.
[49] X. Wang, G. Qin, X. Liang, W. Wang, Z. Wang, D. Liao, L. Zhong, R. Zhang, Y. X. Zeng, Y. Wu, T. Kang, Targeting the CK1alpha/CBX4 axis for metastasis in osteosarcoma, Nat. Commun. 11 (1) (2020) 1141.
[50] Y. Yamakawa, H. Tazawa, J. Hasei, S. Osaki, T. Omori, K. Sugiu, T. Komatsubara, K. Uotani, T. Fujiwara, A. Yoshida, T. Kunisada, Y. Urata, S. Kagawa, T. Ozaki, T. Fujiwara, Role of zoledronic acid in oncolytic virotherapy: promotion of antitumor effect and prevention of bone destruction, Cancer Sci. 108 (9) (2017) 1870–1880.